

SNS Junctions With Bilayer Graphene

Master's Thesis

by

Umut Nefta Kanilmaz

Submission date: 25. February 2018

Advisor: PD Dr. Igor Gornyi
Co-Advisor: Prof. Dr. Alexander Mirlin

Ich erkläre hiermit, dass die Arbeit selbstständig angefertigt, alle benutzten Quellen und Hilfsmittel vollständig und genau angegeben und alles kenntlich gemacht wurde, das aus Arbeiten anderer unverändert oder mit Abänderungen entnommen ist.

Karlsruhe, den 23. Februar 2018

Umut Nefta Kanilmaz

Deutsche Zusammenfassung

Motivation

Als Graphen theoretisch untersucht und seine Transporteigenschaften vorhergesagt wurden, war die Möglichkeit seiner Existenz noch sehr umstritten. Das Mermin-Wagner-Theorem verbot die Existenz von langreichweitiger Ordnung in niedrigdimensionalen Systemen [1].

Es war daher ein wissenschaftlicher Durchbruch, als 2004 die heutigen Nobelpreisträger Andre Geim und Konstantin Novoselov in Manchester Graphen erfolgreich herstellen konnten [2]. Mit den ersten erfolgreichen Transportmessungen, [3] und [4], konnte die zuvor vorhergesagte relativistische Natur der Ladungsträger [5] bestätigt werden. Die Messung des Quanten-Hall-Effekts in Graphen ergab eine halbzählig Wiederkehr der Hall-Plateaus. Dieses Ergebnis bestätigte, dass sich die Ladungsträger in Graphen wie Dirac-Elektronen verhalten. Die relativistische Eigenschaft der Dirac-Elektronen zeigt sich im Spektrum: In der Nähe der K-Punkte, den Eckpunkten der ersten Brillouin-Zone, weist Graphen eine lineare Dispersionsrelation auf. Dieses lineare Verhalten führt zu sehr guten Ladungsträgernmobilität. Das Graphen-Spektrum ist weiterhin auffällig, weil sich Valenz- und Leitungsband an den besagten K-Punkten berühren – Graphen bildet somit einen Halbleiter mit verschwindender Bandlücke.

Die außergewöhnlichen elektronischen Leitungseigenschaften, die beeindruckenden Zugfestigkeit, kombiniert mit einer sehr geringen Flächenmasse macht Graphen zu einem interessanten Kandidaten für die Anwendung in der Computerindustrie [6] oder beispielsweise in der Batterietechnik [7].

Seine Eigenschaften als Halbleiter sind von besonderer Bedeutung in industriellen Anwendungen, aber auch in der Grundlagenforschung. Um die Anwendung in komplexen elektronischen Schaltungen zu ermöglichen muss man die Leitungseigenschaften lokal beeinflussen können. In einer einlagigen Schicht von Graphen gestaltet sich dies schwierig. Die Leitfähigkeit sinkt niemals unter einen bestimmten Wert von e^2/h und es ist nicht möglich, die Ladungsträger in Graphen einzuschränken [8]. Für dieses Problem verspricht doppelagiges Graphen (BLG) Abhilfe. Wenn BLG einem elektrostatischen Feld ausgesetzt wird, haben die beiden Schichten jeweils ein leicht unterschiedliches Potential. Das führt dazu, dass sich im BLG-Spektrum eine Bandlücke abhängig von der Stärke des elektrischen Feldes öffnen lässt. Das legt die Vermutung nahe, dass bei Transportmessungen mit BLG ein isolierender Zustand erreicht werden könnte.

Transportmessung an Supraleiter-BLG-Supraleiter-Schaltungen – eine Schaltung bestehend einer BLG-Fläche, die an den Seiten mit zwei Supraleitern kontaktiert ist – finden nicht den erwarteten isolierenden Zustand [9]. Durch Messung des kritischen Stroms I_c in Abhängigkeit des angelegten Magnetfeldes B konnte Rückschluss auf die Verteilung der Stromdichte innerhalb der Probe getroffen werden. Anhand der Ergebnisse der Stromdichteverteilung wurde die Vermutung aufgestellt, dass Stromtransport durch Kanäle an den Kanten der Probe für die endliche Leitfähigkeit der Probe verantwortlich seien.

Am Institut für Nanotechnologie in der Arbeitsgruppe von Ralph Kruppke werden Supraleiter-BLG-Supraleiter-Schaltungen mit einem sogenannten *weak link*, also einer Engstelle in der Probe, durch die der Strom passieren muss, untersucht. Die experimentelle Untersuchung dieses *weak links*, der die Form eines Quanten-Punkt-Kontaktes hat, wird von einer analytischen Untersuchung des Kontakts im Rahmen einer quasiklassischen Transporttheorie und einer numerischen Untersuchung mittels Tight-Binding-Methode gestützt. Die Ergebnisse dieser Untersuchung sind in [10] veröffentlicht.

Gliederung der Arbeit

Die vorliegende Arbeit beschäftigt sich mit der Physik solcher Supraleiter-Normalleiter-Supraleiter-Schaltungen (SNS-Schaltungen). Der Suprastrom für den QPC-Aufbau wird im Kontext dieser quasiklassischen Transporttheorie untersucht. Die Ergebnisse der Untersuchung werden durch die Berechnung der Supraströme mittels Tight-Binding-Methode ergänzt.

In Kapiteln 2 und 3 werden die Grundlagen aufbereitet, die zum Verständnis dieser Arbeit notwendig sind. In Kapitel 2 werden Prozesse näher betrachtet, die an der Grenzfläche von Supraleitern und Normalleitern relevant sind. Zu nennen ist hier insbesondere die Andreev-Reflektion. Darauf aufbauend wird erläutert, wie es in einer SNS-Schaltung zu Stromfluss kommen kann. Kapitel 3 geht auf Details der Tight-Binding-Methode ein und erläutert den Streumatrix-Ansatz. Zunächst wird der Tight-Binding-Hamiltonian für Graphen und BLG hergeleitet und darauf aufbauend der Modell-Hamiltonian für das QPC-System erklärt. Die experimentellen Fragestellungen, die für diese Arbeit relevant sind, werden in Kapitel 4 eingeführt. Die experimentellen Befunde der SNS-Schaltung mit einem QPC-Aufbau werden vorgestellt und diskutiert.

Die Ergebnisse, die für den Suprastrom im Rahmen der quasiklassischen Transporttheorie folgen, werden in Kapitel 5 vorgestellt. Ein zentrales Ergebnis ist, dass der Übergang von einem oszillierendem zu einem Gauss-förmigen Muster in Übereinstimmung mit den experimentellen Befunden gefunden wird. Weiterhin wird der Stromtransport entlang der Kanten der Probe im Rahmen dieser Transporttheorie untersucht: Die Berechnungen zeigen einerseits, wie der kritische Strom von Randkanälen beeinflusst wird und andererseits, dass in diesem speziellen Aufbau Transport entlang dieser Kanäle unwahrscheinlich ist.

In Kapitel 6 wird neben dem QPC-Aufbau noch ein weiterer, wellenleiterförmiger Aufbau mit Tight-Binding-Modellen untersucht. Die berechneten Ergebnisse für Suprastrom und Leitfähigkeit werden präsentiert und es wird auf den Einfluss von Unordnung in der Probe und Defekte an den Kanten eingegangen. Die berechneten Ergebnisse für den QPC-Aufbau decken sich gut mit den experimentellen Befunden.

Ergebnisse

Das zentrale Ergebnis dieser Arbeit ist, dass

$$J(\tilde{\chi}(y_1, y_2), \phi) \propto \int \int_{-W/2}^{W/2} dy_1 dy_2 \frac{\mathcal{J}(\tilde{\chi}(y_1, y_2))}{\left(1 - \left(\frac{y_1 - y_2}{L}\right)^2\right)^2} \quad (1)$$

Die Potenz im Nenner für den Strom durch die SNS junction geht mit der Potent von 2. Dies widerspricht dem Ergebnis von [11]. Die Stromdichte für das QPC wurde aufgestellt, sie lautet

$$J(\tilde{\chi}(y_1, y_2), \phi) \propto \int \int_{-W/2}^{W/2} dy_1 dy_2 \frac{\cos\left(\frac{\pi\phi}{W}(y_1 + y_2)\right)}{\left[1 + \left(\frac{y_1 - y_2}{L}\right)^2\right]^2}, \quad (2)$$

Der kritische Strom wurde für den Grenzfall $\phi \rightarrow 0$, in dem eine parabolische Funktion abhängig von W/L für das QPC gefunden wurde, ausgewertet. Im anderen Grenzfall, $\phi \rightarrow \infty$, wird der exponentielle Abfall für große ϕ korrekt wiedergegeben. Ebenfalls wurde das Verhalten der Randströme im Rahmen der quasi-klassischen Näherung untersucht. Es zeigt sich, dass für verschiedenen Tranmissionskoeffizienten \mathcal{T}_e der Kante und \mathcal{T}_q des QPC der kritische Strom durch einen Faktor

$$\mathcal{C} = \frac{|\mathcal{T}_q/\mathcal{T}_e + \cos(\pi\phi)/2|}{\mathcal{T}_q/\mathcal{T}_e + 1/2} \quad (3)$$

moduliert wird. Diese Modulation zeigt sich schon ab einem Wert von $\mathcal{T}_e/\mathcal{T}_q = 1/100$. Dies ist ein starker Hinweis darauf, dass in den beobachteten Daten keine Kantenströme zu finden sind.

Ausblick

Die im Rahmen dieser Arbeit vorgestellte Transporttheorie kann in verschiedenen Aspekten erweitert werden. Es wurde demonstriert, dass diese Theorie einen *weak link* in Form eines QPC gut modellieren kann. Es ist deshalb denkbar, ähnliche Formen von weak links zu modellieren.

In dieser Arbeit wurde ein kurzer SNS-Aufbau betrachtet. Das hat bestimmte Näherungen, die die Rechnungen vereinfachen, als Konsequenz. Für den anderen Grenzfall einer langen SNS-Schaltung ist zum einen Streuung an den Kanten ein wichtiger Bestandteil zum Stromtransport und muss daher berücksichtigt werden. Zum anderen müssen Terme höherer Ordnung für die Berechnung der Stromdichte berücksichtigt werden. Somit ist die einfachste Form der Josephson-Gleichung in diesem Fall nicht mehr ausreichend.

Bisher wurde lediglich Andreev Retroreflexion betrachtet, bei der das Loch auf annähernd der gleichen Trajektorie reflektiert wird wie das Elektron, nur mit umgekehrten Impuls. Im Fall von Graphen überwiegt allerdings der Prozess der Specular Andreev reflection, bei dem das reflektierte Loch nicht auf der gleichen Trajektorie zurückwandert. Die quasiklassische Theorie kann auch auf diesen Fall erweitert werden und damit Graphen-spezifische Eigenschaften berücksichtigen.

Die numerischen Simulationen mit **kwant** können erweitert werden. Die vorliegende Arbeit implementiert das BLG System als de facto zweidimensional. Realistische experimentelle Aufbauten sind jedoch komplexer: Zum einen sind sie dreidimensional und zum anderen wird die räumliche Verteilung der elektrostatischen Felder zu vereinfacht angenommen. Eine Kombination aus Berechnung dieser Felder über numerische Verfahren und Simulationen mit **kwant** kann Experimente vollständiger beschreiben.

Contents

1	Introduction	1
2	A Framework For The Quasi-classical Model	3
2.1	Theory Of Superconductivity	3
2.2	The Interface Between A Superconductor And Normal Conductor: Andreev Reflection	6
2.3	Theory Of SNS Junctions	9
2.4	SNS Junction And The Josephson Effect	11
2.5	Graphene And Superconductivity: Specular Andreev Reflection	12
3	A Framework For The Numerical Analysis	15
3.1	Tight Binding Model For Graphene	15
3.1.1	Monolayer Graphene	16
3.1.2	Bilayer Graphene	17
3.1.3	Tight Binding Models And <code>kwant</code>	18
3.2	Random Matrix Theory For Transport	19
3.2.1	Fundamental Idea	19
3.2.2	Supercurrent In An SNS Junction	20
4	Experimental Motivation	23
4.1	Introduction	23
4.2	Normal State Analysis	24
4.3	Superconducting State	25
5	Analytical Model	27
5.1	Foundation Of The Quasi-classical Model	27
5.2	Plane Set-up: Calculation Of The Critical Current	28
5.3	Calculation Of The QPC Critical Current	33
5.4	QPC Edge Current	36
5.5	Barrier With Finite Split Width: Transition To The QPC Set-up	38
6	Numerical Results	41
6.1	QPC	41
6.2	Half-Barrier	42
6.3	Wave-guide	43
7	Conclusion And Outlook	45
Bibliography		47

1

Introduction

Graphene, Superconductivity, And Quantum Point Contacts

In the year 1947, when graphene was first theoretically investigated and its transport properties were predicted by Phil Wallace [12], the possibility of its existence was still very controversial. The Mermin-Wagner theorem prohibited the existence of long-range order in low-dimensional systems [1].

It was therefore a scientific breakthrough when today's Nobel Prize winners Andre Geim and Konstantin Novoselov were able to successfully produce graphene in Manchester in 2004 [2]. With the first successful transport measurements, [3] and [4], the previously predicted relativistic nature of charge carriers [5] could be confirmed. The measurement of the quantum Hall effect in graphene revealed a half-numbered return of the Hall plateaus. This result confirmed that the charge carriers in graphene behave like Dirac electrons.

The relativistic property of the Dirac electrons is shown in the spectrum. Near the K-points, the corner points of the first Brillouin zone, graphene has a linear dispersion relation. This linear behaviour leads to a very good charge carrier mobility. The graphene spectrum is still noticeable because valence and conduction bands touch each other at the K points – graphene thus forms a semiconductor with a disappearing band gap.

The extraordinary electronic conduction properties, the impressive tensile strength combined with a very low surface mass makes graphene an interesting candidate for application in the computer industry [6] or, for example, in battery technology [7].

Its properties as a semiconductor are of particular importance in industrial applications, but also in fundamental research. In order to enable application in complex electronic circuits, it must be possible to control the conductive properties locally. This is difficult to do in a single layer of graphene. The conductivity never drops below a certain value of e^2/h , and it is not possible to confine the charge carriers in graphene [8]. Double-layer graphene (BLG) promises to be a solution to this problem. When BLG is exposed to an electrostatic field, the two layers each have a slightly different potential. This means that a band gap can be opened in the BLG spectrum, depending on the strength of the electric field. This suggests that an isolating state could be achieved during transport measurements with BLG.

In a superconductor-BLG-superconductor junction – a junction consisting of a BLG surface contacted at the sides with two superconductors – the expected insulating state could not be found in transport measurements [9]. By measuring the critical current I_c as a function of the applied magnetic field B , the distribution of the current density within the sample can be found. Based on the results of the current density distribution, it was assumed that current transport through channels at the edges of the sample is responsible for the finite conductivity of the sample.

At the Institute of Nanotechnology in the research group of Ralph Kruppke, superconductor-BLG-superconductor junctions are investigated with a so-called *weak link*, i. e. a constriction in the sample through which the current must pass. This weak link has the form of a quantum-point-contact (QPC) and its experimental investigation is supported by an analytical study, which is presented in this thesis. The present work deals with the question of how the experimental data can be explained in the context of a quasi-classical transport theory. To this end, existing approaches have been reviewed and an adjusted approach has been proposed for the QPC set-up. The results of the quasi-classical analysis of the QPC, along with the experimental data and numerical simulations, have been published in [?].

Structure Of This Thesis

This thesis deals with the physics of such superconductor-normal metal-superconductor junctions (SNS junctions). The supercurrent for the QPC structure is explored within the framework of this quasi-classical transport theory. The results of the investigation are supplemented by the calculation of the supercurrent using the tight-binding method.

In chapters 2 and 3 the basics necessary for understanding this work are presented. In chapter ?? processes that are relevant at the interface of superconductors and normal conductors are examined in more detail. The Andreev reflection should be mentioned in particular. Based on this, it is explained how current flow can occur in an SNS junction. Chapter 3 discusses details of the tight binding method and explains the scattering matrix approach. First, the tight-binding Hamiltonian for graphene and BLG is derived and then the model Hamiltonian for the QPC system is explained.

The experimental questions relevant to this work are introduced in chapter 4. The experimental findings of the SNS junction with a QPC structure for both the normal state and the superconducting state are presented and discussed.

The results for the supercurrent obtained within the framework of quasi-classical transport theory are presented in chapter 5. A key result is that the transition from an oscillating to a Gaussian bell-shaped pattern is found in accordance with the experimental findings. Furthermore, the current transport along the edges of the sample is investigated within the framework of this transport theory: The calculations show how the critical current is influenced by boundary channels and also that transport along these channels is unlikely in this particular configuration.

In chapter 6 a further set-up, the QPC set-up and a waveguide-shaped structure, are examined. For this chapter, calculations are made using tight-binding models. The calculated results for supercurrent and conductivity are presented and the influence of disorder in the sample and defects at the edges are discussed. The calculated results for the QPC set-up are well in line with the experimental findings.

2 A Framework For The Quasi-classical Model

2.1 Theory Of Superconductivity

The discovery of the isotope effect in 1950 revealed that not only lattice electrons but rather the whole lattice determines the superconducting properties of a solid. Experiments measuring the critical temperature T_c of different mercury isotopes showed that, indeed, there is a relation between the isotope mass and T_c . Herbert Fröhlich was then the first to introduce a new concept to explain superconductivity. He showed that a phonon-mediated interaction between electrons and the lattice could lead to an attractive long-range interaction of electrons in the lattice. Figuratively speaking, an electron passing through the crystal lattice will polarize it by attracting the positive ions. It leaves a deformed lattice, which will then attract a second electron. An effective attractive interaction between these two electrons is thereby created. In 1956, Cooper showed that the electronic ground state, the Fermi sea at $T = 0$, is unstable if a weak attractive interaction is taken into account. This layed the foundation of the BCS theory [13], the first successful microscopic theory after the discovery of superconductivity in 1911 by Heike Kammerling Onnes.

Preliminaries

The BCS Hamiltonian reads

$$H = H_0 + H_1 \quad (2.1)$$

$$H_0 = \sum_{\mathbf{k}, \sigma} \xi_{\mathbf{k}} c_{\mathbf{k}\sigma}^{\dagger} c_{\mathbf{k}\sigma} \quad (2.2)$$

$$H_1 = \frac{1}{N} \sum_{\mathbf{k}, \mathbf{k}'} V_{\mathbf{k}\mathbf{k}'} c_{\mathbf{k}\uparrow}^{\dagger} c_{-\mathbf{k}\downarrow}^{\dagger} c_{-\mathbf{k}'\downarrow} c_{\mathbf{k}'\uparrow} \quad (2.3)$$

The operators $c_{\mathbf{k}, \sigma}^{\dagger}$ and $c_{\mathbf{k}, \sigma}$ are fermion operators that create or annihilate an electron with momentum \mathbf{k} and spin σ . The first term in the Hamiltonian H is the unperturbed electron Hamiltonian H_0 with parabolic energy dispersion $\xi_{\mathbf{k}}$. The second term is the interaction Hamiltonian H_1 , expressing the scattering of two electrons from $(\mathbf{k}' \downarrow, -\mathbf{k}' \uparrow)$ to $(\mathbf{k} \uparrow, -\mathbf{k} \downarrow)$. The interaction potential $V_{\mathbf{k}, \mathbf{k}'}$ exchanges the scattering for electrons with energy $|\xi_{\mathbf{k}}| \lesssim \hbar\omega_D$. The Hamiltonian in eq. (2.1) can be simplified by a mean-field approximation. In this approximation, an operator A is expressed by a sum of its statistical mean $\langle A | A \rangle$ and small statistical fluctuations δA . Since the fluctuations

are assumed to be small, terms with $\mathcal{O}((\delta A)^2)$ can be neglected.

$$\begin{aligned} A &= \langle A \rangle + \delta A, \quad B = \langle B \rangle + \delta B \\ AB &= \langle A \rangle \langle B \rangle + \langle A \rangle \delta B + \langle B \rangle \delta A + \underbrace{\delta A \delta B}_{\approx 0} \end{aligned} \quad (2.4)$$

Using $\delta A = A - \langle A \rangle$ and inserting this back into eq. (2.4) leads to

$$AB = \langle A \rangle B + \langle B \rangle A - \langle A \rangle \langle B \rangle. \quad (2.5)$$

This approximation is applied to the interaction part H_1 in eq. (2.3), replacing

$$A = c_{\mathbf{k}\uparrow}^\dagger c_{-\mathbf{k}\downarrow}^\dagger, \quad B = c_{-\mathbf{k}'\downarrow} c_{\mathbf{k}'\uparrow}. \quad (2.6)$$

The result is the BCS-Hamiltonian

$$H_{\text{BCS}} = \sum_{\mathbf{k},\sigma} \xi_{\mathbf{k}} c_{\mathbf{k}\sigma}^\dagger c_{\mathbf{k}\sigma} - \sum_{\mathbf{k}} \Delta_{\mathbf{k}}^* c_{-\mathbf{k}\downarrow} c_{\mathbf{k}\uparrow} - \sum_{\mathbf{k}} \Delta_{\mathbf{k}} c_{\mathbf{k}\uparrow}^\dagger c_{-\mathbf{k}\downarrow}^\dagger + \text{const.} \quad (2.7)$$

where

$$\Delta_{\mathbf{k}} := -\frac{1}{N} \sum_{\mathbf{k}'} V_{\mathbf{k}\mathbf{k}'} \langle c_{-\mathbf{k}'\downarrow} c_{\mathbf{k}'\uparrow} \rangle \quad (2.8)$$

$$\Delta_{\mathbf{k}}^* := -\frac{1}{N} \sum_{\mathbf{k}'} V_{\mathbf{k}\mathbf{k}'} \langle c_{\mathbf{k}'\uparrow}^\dagger c_{-\mathbf{k}'\downarrow}^\dagger \rangle \quad (2.9)$$

The BCS-Hamiltonian in eq. (2.7) can be diagonalized using the Bogoliubov transformation. The aim is to express the Hamiltonian in the basis of new fermion operators. These new operators will describe quasiparticles, which are a linear combination of $c_{\mathbf{k},\sigma}^\dagger$ and $c_{\mathbf{k},\sigma}$,

$$\begin{pmatrix} \gamma_{\mathbf{k}\uparrow} \\ \gamma_{-\mathbf{k}\downarrow}^\dagger \end{pmatrix} = \begin{pmatrix} u_{\mathbf{k}}^* & -v_{\mathbf{k}} \\ v_{\mathbf{k}}^* & u_{\mathbf{k}} \end{pmatrix} \begin{pmatrix} c_{\mathbf{k}\uparrow} \\ c_{-\mathbf{k}\downarrow}^\dagger \end{pmatrix} \quad (2.10)$$

Evaluating the fermion anticommutation relation using the transformation above yields

$$\left\{ \gamma_{\mathbf{k}\uparrow}, \gamma_{\mathbf{k}\uparrow}^\dagger \right\} = \dots = |u_{\mathbf{k}}|^2 + |v_{\mathbf{k}}|^2 \stackrel{!}{=} 1 \quad (2.11)$$

and will lead to the inverse transformation of eq. (2.1). Inserting the inverse transformation into the BCS-Hamiltonian in eq. (2.7) will give the coefficients $u_{\mathbf{k}}$, $v_{\mathbf{k}}$ from eq. (2.1) and finally yield to the diagonalized form of the BCS-Hamiltonian

$$H_{\text{BCS}} = \sum_{\mathbf{k}\sigma} E_{\mathbf{k}} \gamma_{\mathbf{k}\sigma}^\dagger \gamma_{\mathbf{k}\sigma} \quad (2.12)$$

$$E_{\mathbf{k}} := \sqrt{\xi_{\mathbf{k}}^2 + |\Delta_{\mathbf{k}}|^2} \quad (2.13)$$

For a fixed energy $E_k \stackrel{!}{=} \epsilon$, eq. (2.13) gives two possible values for ξ_k :

$$\xi_{\mathbf{k}} = \pm \sqrt{\epsilon^2 - |\Delta_{\mathbf{k}}|^2}. \quad (2.14)$$

Knowing that $k^2 = k_F^2 \pm 2m\sqrt{\epsilon^2 + |\Delta_k|^2}\hbar^2$, one can calculate the group velocity as

$$v_g = \frac{d\epsilon}{d(\hbar k)} = \pm v_F \frac{\sqrt{\epsilon^2 - |\Delta|^2}}{\epsilon}. \quad (2.15)$$

The group velocity is positive for excitations outside the Fermi surface and negative for excitations inside. Therefore, the positive solution is a particle-like excitation, and the negative solution is a hole-like excitation. Figure 2.1 shows the excitation spectrum of particles and holes from the BCS theory.

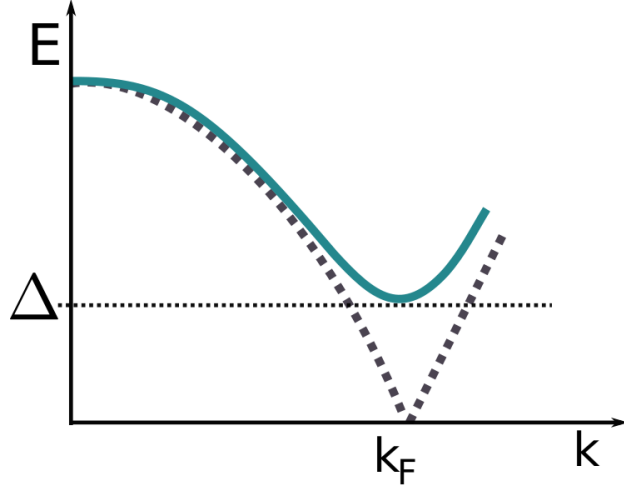


Figure 2.1: Excitations from BCS theory. The dashed line is the normal state dispersion relation ($\Delta = 0$). The solid line is the dispersion relation for the superconducting state ($\Delta \neq 0$), where no excitations with energies $\epsilon < \Delta$ are present.

Bogoliubov de Gennes Hamiltonian

The ansatz for the BCS ground state used by Bardeen, Cooper and Schrieffer is based on the concept of Cooper pairs. It is a direct consequence of the instability in the ground state through the attractive interaction. The BCS theory proposes a BCS ground state built on eigenstates of the single-particle Hamiltonian H_0 from eq. (2.2), leading to a ground state that consists of a linear combination of pair states.

$$|\psi_{\text{BCS}}\rangle = \prod_{\mathbf{k}} (u_{\mathbf{k}} + v_{\mathbf{k}} c_{\mathbf{k}\uparrow}^\dagger c_{-\mathbf{k}\downarrow}^\dagger) |\text{vac}\rangle \quad (2.16)$$

$$H_{\text{BCS}} |\psi_{\text{BCS}}\rangle = E_{\text{BCS}} |\psi_{\text{BCS}}\rangle \quad (2.17)$$

In most cases however, a more realistic set-up or inhomogeneous system cannot be described in terms of eigenfunctions of H_0 . With a vector potential $\mathbf{A} \neq 0$, for example, time reversal symmetry is not given any more. The characteristic length scale is the superconducting coherence length ξ_0 . If a system is varying slowly over a length scale $l \approx \xi_0$, a spatially dependent, more general Hamiltonian is needed. In order to find an adequate expression for such a spatially dependent Hamiltonian, the following spinor is introduced

$$|\Psi_{\mathbf{k}}\rangle = \begin{pmatrix} |\Psi_{\mathbf{k}_1}\rangle \\ |\Psi_{\mathbf{k}_2}\rangle \end{pmatrix} := \begin{pmatrix} c_{\mathbf{k},\uparrow}^\dagger \\ c_{-\mathbf{k},\downarrow}^\dagger \end{pmatrix} |\psi_{\text{BCS}}\rangle \quad (2.18)$$

In this basis $\{|\Psi_{\mathbf{k}_1}\rangle, |\Psi_{\mathbf{k}_2}\rangle\}$, the Hamiltonian (2.7) takes the form known as the Bogoliubov de Gennes Hamiltonian

$$H_{\text{BdG}}(\mathbf{k}) = \begin{pmatrix} \xi_{\mathbf{k}} & -\Delta_{\mathbf{k}} \\ -\Delta_{\mathbf{k}}^* & -\xi_{\mathbf{k}} \end{pmatrix}. \quad (2.19)$$

The energies are measured relative to $E_{\mathbf{k}}$ and a constant E_{BCS} has been neglected. This Hamiltonian form eq. (2.19) has the eigenvalues

$$\pm E_{\mathbf{k}} = \pm \sqrt{\xi_{\mathbf{k}}^2 + |\Delta_{\mathbf{k}}|^2}. \quad (2.20)$$

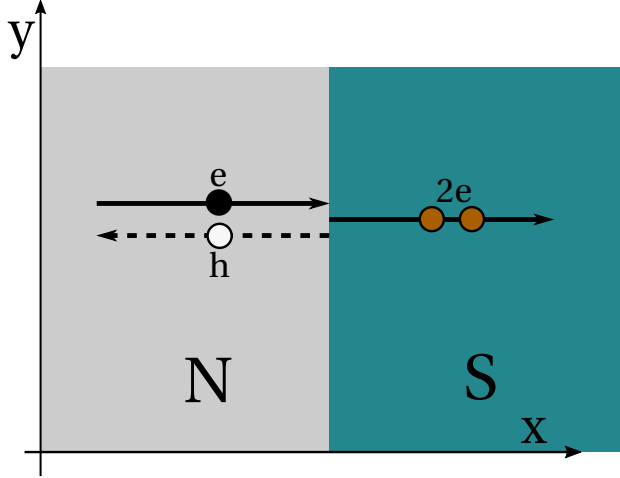


Figure 2.2: Andreev reflection at an NS interface. An incoming electron is Andreev reflected into a hole with opposite momentum, and a Cooper pair condenses into the superconductor. The interface is modelled as a sharp edge.

To finally arrive at the spatially dependent form of eq. (2.19), the Hamiltonian is Fourier-transformed.

$$H_{\text{BdG}}(\mathbf{r}) := \frac{1}{N} \sum_{\mathbf{k}} e^{i\mathbf{k}\cdot\mathbf{r}} H_{\text{BdG}}(\mathbf{k}) \quad (2.21)$$

$$= \begin{pmatrix} H_0(\mathbf{r}) & -\Delta(\mathbf{r}) \\ -\Delta^*(\mathbf{r}) & -H_0(\mathbf{r}) \end{pmatrix} \quad (2.22)$$

$H_0(\mathbf{r})$ is the free Hamiltonian. Corresponding Schrödinger equations are called BdG-equations:

$$H_{\text{BdG}}(\mathbf{r}) \Psi(\mathbf{r}) = E \Psi(\mathbf{r}) \quad (2.23)$$

$$\Psi(\mathbf{r}) = \begin{pmatrix} \Psi_1(\mathbf{r}) \\ \Psi_2(\mathbf{r}) \end{pmatrix}. \quad (2.24)$$

2.2 The Interface Between A Superconductor And Normal Conductor: Andrev Reflection

Now that the principles of BCS theory have been established, the physical effects at the interface between a superconductor and a normal metal are to be outlined.

The most important detail when modelling the interface between a superconductor (S) and a normal metal (N) is the superconducting order parameter $\Delta(\mathbf{r})$. It is present in the superconducting region and zero in a normal metal. To keep the model as simple as possible, a step-like behaviour is assumed. This means that for an interface placed at $x = 0$, the superconducting order parameter becomes a function of x and can be written as

$$\Delta(x) = \theta(x) \Delta_0. \quad (2.25)$$

How does the eigenvalue problem (2.23) with the potential (2.25) differ from a quantum mechanical step potential set-up? The formalism is virtually identical, but there is a subtle and important difference in the results. In the normal region, there are electrons, whereas in the superconducting

regions, there is a condensate of Cooper pairs. A normal electron can be reflected at the interface as a hole and an additional Cooper pair can be created in the superconducting region (see figure 2.2). By solving the Bogoliubov-de-Gennes equation in (2.23), this picture becomes clearer. This equation needs to be solved both for the normal and the superconducting region. When treating this problem quantum-mechanically, energies below and above the gap need to be considered independently. The resulting wave functions have to be continuous at the interface. Depending on the region, the gap parameter in the Hamiltonian in eq. (2.22) is either zero or Δ_0 .

Semi-classical Approximation: Andreev Equations

With the NS interface, the gap parameter varies slowly over scales of k_F^{-1} , and it may vary over scales of the coherence length ξ_0 . Because k_F^{-1} is a good length scale for this problem, the equations above can be simplified:

$$\Psi(\mathbf{r}) = e^{i\mathbf{k}_F \cdot \mathbf{r}} \begin{pmatrix} u(\mathbf{r}) \\ v(\mathbf{r}) \end{pmatrix}. \quad (2.26)$$

Since $u(\mathbf{r})$ and $v(\mathbf{r})$ vary slowly over distances of order k_F^{-1} , the second derivative with respect to \mathbf{r} can be neglected. This approach is called the semi-classical approximation, which allows to transform the BdG eqs. (2.23) into the Andreev equations

$$-i\hbar v_F \nabla u(\mathbf{r}) + \Delta(\mathbf{r}) v(\mathbf{r}) = \epsilon u(\mathbf{r}) \quad (2.27)$$

$$i\hbar v_F \nabla v(\mathbf{r}) + \Delta^*(\mathbf{r}) u(\mathbf{r}) = \epsilon v(\mathbf{r}). \quad (2.28)$$

These equations are significantly easier to handle than the BdG-equations, since they describe a first-order problem.

Consider an incoming particle from the left half-space $x < 0$, travelling towards the superconducting interface at $x = 0$, assuming that both the normal region and the superconductor have the same Fermi velocity v_F . The one-dimensional Andreev equations for the NS interface read

$$-i\hbar v_{F,x} \frac{d}{dx} u(x) + \Delta(x) v(x) = \epsilon u(x) \quad (2.29)$$

$$i\hbar v_{F,x} \frac{d}{dx} v(x) + \Delta^*(x) u(x) = \epsilon v(x). \quad (2.30)$$

In the normal region (for $x < 0$), the superconducting gap parameter decreases to zero on a length scale shorter than ξ_0 . Therefore, the step-like approximation from eq. (2.25) holds. In the normal region, the coefficients $u(x)$ and $v(x)$ are independent. The ansatz contains an incident wave with unity amplitude and a reflected hole with amplitude r .

$$\Psi_N(x) = \begin{pmatrix} u(x) \\ v(x) \end{pmatrix}_N = e^{ik_N x} \begin{pmatrix} 1 \\ 0 \end{pmatrix} + r e^{-ik_N x} \begin{pmatrix} 0 \\ 1 \end{pmatrix}, \quad (2.31)$$

where, writing $v_x \equiv v_{F,x}$,

$$k_N = \frac{\epsilon}{\hbar v_x}. \quad (2.32)$$

In the superconducting region, the solution for the wave function has the form

$$\Psi_S(x) = \begin{pmatrix} u(x) \\ v(x) \end{pmatrix}_S = t e^{ik_S x} \begin{pmatrix} u_0 \\ v_0 \end{pmatrix}. \quad (2.33)$$

The expression for the wave vector k_S depends on the energy of the incoming particle, which can be either *above* or *below* the gap.

For high energies *above* the gap, $\epsilon > |\Delta|$, the wave vector is

$$k_S = \frac{\sqrt{\epsilon^2 - \Delta^2}}{\hbar v_x} \quad (2.34)$$

If the energy of the incoming particle is higher than the gap energy, it can be transmitted into the superconductor. The amplitude t therefore is the transmission probability. The coherence factors u_0, v_0 can be found by solving the BdG equations within the BCS framework. Matching the boundary conditions at the interface yields

$$r = \frac{v_0}{u_0}, \quad t = \frac{1}{u_0}. \quad (2.35)$$

Normalizing the wave functions leads to

$$|r|^2 + (u_0^2 - v_0^2)|t|^2 = 1 \quad (2.36)$$

Since ϵ is the energy relative to the Fermi energy, the normal wave vector from eq. (2.31) can be written in terms of

$$\mathbf{q}_\pm = \left(k_F \pm \frac{\epsilon}{\hbar v_F} \right) \hat{\mathbf{k}}_F \quad (2.37)$$

$$\Psi_N(\mathbf{r}) = e^{i\mathbf{q}_+ \cdot \mathbf{r}} \begin{pmatrix} 1 \\ 0 \end{pmatrix} + a e^{i\mathbf{q}_- \cdot \mathbf{r}} \begin{pmatrix} 0 \\ 1 \end{pmatrix}. \quad (2.38)$$

Using eq. (2.37), one can determine the trajectory of the reflected hole to coincide with the trajectory of the incoming electron. The change in momentum,

$$\Delta p_x = -\frac{2e}{v_x}, \quad (2.39)$$

is small. The components p_y, p_z are conserved, therefore the trajectory of the reflected hole is almost the same as the trajectory of the incoming electron.

For energies *below* the gap, $\epsilon < |\Delta|$, there are no states available inside the gap. Therefore, the wave function decays inside the superconductor.

The wave function is

$$\begin{pmatrix} u(x) \\ v(x) \end{pmatrix}_S = t e^{-\tilde{k}_S x} \begin{pmatrix} u_0 \\ v_0 \end{pmatrix}, \quad (2.40)$$

where

$$\tilde{k}_S = \frac{\sqrt{\Delta^2 - \epsilon^2}}{\hbar v_x}. \quad (2.41)$$

For sub-gap energies, the amplitudes of the normal wave functions are slightly modified:

$$r = \frac{v_0}{\tilde{u}_0} \quad (2.42)$$

and

$$\text{and } t = \frac{1}{\tilde{u}_0}, \quad (2.43)$$

where

$$\tilde{u}_0 = \frac{1}{\sqrt{2}} \left(1 + i \frac{\sqrt{|\Delta|^2 - \epsilon^2}}{\epsilon} \right) \quad \text{and} \quad \tilde{v}_0 = \frac{1}{\sqrt{2}} \left(1 - i \frac{\sqrt{|\Delta|^2 - \epsilon^2}}{\epsilon} \right). \quad (2.44)$$

In this case, it holds that

$$|r|^2 = 1 \quad (2.45)$$

In other words, there are no transmitted particles and all particles are Andreev reflected.

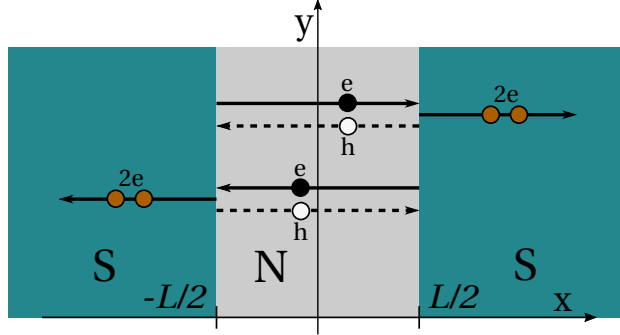


Figure 2.3: An SNS junction of width W . Electrons are indicated as solid arrows, holes as dashed ones. An electron (hole) is Andreev reflected as a hole (electron) at one side, which then again is reflected at the other side. In this way, Andreev bound states form in the junction.

2.3 Theory Of SNS Junctions

So far, only NS interfaces have been considered. The same procedure can be applied to superconductor - normal metal - superconductor (SNS) junctions: A sandwich structure of a superconductor on the left side, a normal region in the middle and a superconductor on the right side, as visualized in figure 2.3. At both interfaces, a particle can be Andreev-reflected. Each time an electron is Andreev-reflected at the right side and a hole travels back, a Cooper pair is induced into the right superconductor. In the same manner, a Cooper pair is stolen from the left superconductor when the hole is Andreev-reflected as an electron. This process is illustrated in figure 2.3. As an overall consequence, a supercurrent through the SNS junction can be observed. This process leads to localized electrons with bound states, known as Andreev bound states.

In the following, an SNS junction with normal region at $|x| < W/2$, the right superconductor at $x > +W/2$ and the left superconductor at $x < -W/2$ is considered. The electrons in both superconducting regions and in the normal metal have the same Fermi velocity and there are no insulating barriers between them. This means that W is smaller than the electron mean free path. For short W this implies that the mean free path is larger than the superconducting coherence length. The phase difference between the superconductors is χ , so the right superconductor can be assumed to be characterised by the phase $\chi/2$ and the left one by $-\chi/2$. The semi-classical approximation is used and a wave function with the form

$$\Psi(\mathbf{r}) = e^{i\mathbf{k_F}\mathbf{r}} \begin{pmatrix} u(\mathbf{r}) \\ v(\mathbf{r}) \end{pmatrix}. \quad (2.46)$$

is needed. In the normal region, it holds that

$$\Psi_N(x) = A \cdot \left[e^{ik_N x} \begin{pmatrix} 1 \\ 0 \end{pmatrix} + a e^{-ik_N x} \begin{pmatrix} 0 \\ 1 \end{pmatrix} \right], \quad (2.47)$$

$$k_N = \frac{\epsilon}{\hbar v_x}. \quad (2.48)$$

Assuming that $k_x > 0$, the wave function in the right superconductor ($x > W/2$) is

$$\Psi_S^R(x) = d_1 e^{-\tilde{k}_S x} \begin{pmatrix} \tilde{u}_0 e^{i\chi/4} \\ \tilde{v}_0 e^{-i\chi/4} \end{pmatrix}, \quad (2.49)$$

$$\tilde{k}_S = \frac{\sqrt{|\Delta|^2 - \epsilon^2}}{\hbar |v_x|}. \quad (2.50)$$

For the left superconductor, the wave function is

$$\Psi_S^L(x) = d'_1 e^{\tilde{k}_S x} \begin{pmatrix} \tilde{v}_0 e^{-i\chi/4} \\ \tilde{u}_0 e^{i\chi/4} \end{pmatrix}. \quad (2.51)$$

Applying the continuity condition at the interfaces leads to

$$ae^{-ik_n W} = \frac{\tilde{v}_0}{\tilde{u}_0} e^{-i\chi/2} \quad (2.52)$$

$$ae^{ik_n W} = \frac{\tilde{u}_0}{\tilde{v}_0} e^{i\chi/2}. \quad (2.53)$$

Combining these equations, we find

$$e^{2i(k_n W - \chi/2)} = \frac{\epsilon + i\sqrt{|\Delta|^2 - \epsilon^2}}{\epsilon - i\sqrt{|\Delta|^2 - \epsilon^2}}. \quad (2.54)$$

To simplify this expression, one can introduce

$$\sin \alpha := \frac{\epsilon}{|\Delta|}, \quad -\pi/2 < \alpha < \pi/2 \quad (2.55)$$

Using eq. (2.55), one can rewrite the right hand side of eq. (2.54) in terms of trigonometric functions and gets

$$e^{2i(k_n W - \chi/2)} = e^{-2i\alpha + i\pi}, \quad (2.56)$$

which then leads to

$$\epsilon = \frac{\hbar v_x}{W} \left(\pi \left(l + \frac{1}{2} \right) - \arcsin \frac{\epsilon}{|\Delta|} + \frac{\chi}{2} \right). \quad (2.57)$$

If $k_x < 0$, it holds that

$$\Psi_S^R(x) = d_2 e^{-\tilde{k}_S x} \begin{pmatrix} \tilde{v}_0 e^{i\chi/4} \\ \tilde{u}_0 e^{-i\chi/4} \end{pmatrix} \quad (2.58)$$

For the left superconductor, the wave function is

$$\Psi_S^L(x) = d'_2 e^{\tilde{k}_S x} \begin{pmatrix} \tilde{u}_0 e^{-i\chi/4} \\ \tilde{v}_0 e^{i\chi/4} \end{pmatrix} \quad (2.59)$$

An analogous calculation leads to

$$\epsilon = -\frac{\hbar |v_x|}{W} \left(\pi \left(l - \frac{1}{2} \right) + \arcsin \frac{\epsilon}{|\Delta|} + \frac{\chi}{2} \right) \quad (2.60)$$

The final result for the spectrum is

$$\epsilon = \pm \frac{\hbar |v_x|}{W} \left(\pi \left(l \pm \frac{1}{2} \right) \mp \arcsin \frac{\epsilon}{|\Delta|} + \frac{\chi}{2} \right) \quad (2.61)$$

The upper sign is corresponds to $k_x > 0$ and the lower sign corresponds to $k_x < 0$. Normalizing the wave functions fixes the coefficient in eq. (2.31)

$$|A|^2 = \frac{1}{2(W + k_S^{-1})} = \frac{1}{2} \frac{\sqrt{|\Delta|^2 - \epsilon^2}}{\hbar |v_x| + W \sqrt{|\Delta|^2 - \epsilon^2}}. \quad (2.62)$$

Limit of short junction

For junctions with small width W , such that

$$W \ll \frac{\hbar v_x}{|\Delta|}, \quad \xi \ll W \quad (2.63)$$

holds, where $\xi_0 \sim \hbar v_F / |\Delta|$ is the coherence length. Then, in eq. (2.54) the term with $e^{2ik_n W} \approx 1$ and the spectrum becomes

$$\epsilon = \mp \cos \frac{\chi}{2}, \quad 0 < \chi < \pi. \quad (2.64)$$

Limit of long junction

Long junction, $W \gg \xi_0$, it holds that

$$W \gg \frac{\hbar |v_x|}{|\Delta|}. \quad (2.65)$$

Then the spectrum is given by

$$\epsilon = \pm \frac{\hbar |v_x|}{W} \left(\frac{\chi}{2} - \frac{\pi}{2} \right) + \frac{l\pi\hbar |v_x|}{W}, \quad (2.66)$$

because $\arcsin \frac{\epsilon}{|\Delta|}$ can be neglected.

2.4 SNS Junction And The Josephson Effect

The Josephson effect [14] describes the flow of a supercurrent through two superconducting leads coupled by a weak link. This weak link can be an insulator or a normal conductor. The conventional picture is that the current can be described as a consequence of Cooper pairs tunneling through a barrier. It is also possible to view the current as a consequence of electrons being Andreev reflected, as has been described in section 2.3 from one superconducting leads. The bound states, that from in the junction carry the current from one superconductor to another. A calculation of the Josephson current within the framework presented above, i.e. starting with the BdG Hamiltonian and matching the wave functions at the interface, is presented in [15]. Within the picture of electrons tunnelling through a barrier, the supercurrent density is found from the generalized London equation

$$\mathbf{J}_s(\mathbf{r}, t) = q_s n_s(\mathbf{r}, t) \left(\frac{\hbar}{m_s} \nabla \chi(\mathbf{r}, t) - \frac{q_s}{m_s} \mathbf{A} \right) \equiv \frac{q_s n_s \hbar}{m_s} \gamma(\mathbf{r}, t), \quad (2.67)$$

where q_s are the charge carriers in a superconductor ($q_s = 2e$) and n_s is the density of the superconducting electrons. The supercurrent density is a function of χ . It has a 2π -periodicity and it is zero for $\chi = 0$:

$$J_s(\chi) = J_s(\chi + n2\pi) \quad (2.68)$$

$$J_s(\chi = 0) = J_s(\chi = n \cdot 2\pi) = 0 \quad (2.69)$$

Therefore, the most general solution for the supercurrent density is of the form

$$J_s(\chi) = J_c \sin \chi + \sum_{m=2}^{\infty} J_m \sin(m\chi), \quad (2.70)$$

where J_c is the critical Josephson current density. In most cases however, it is sufficient to only consider the first term, so that

$$J_s(\chi) = J_c \sin \chi \quad (2.71)$$

When including a magnetic field, the phase will become a function of the vector potential \mathbf{A} . By calculating the phase difference $\chi(y_A) - \chi(y_B)$ of two points y_A, y_B along the y -axis the effect of the magnetic field to the Josephson relation can be determined. Using eq. 2.67:

$$\tilde{\chi}(\mathbf{r}) = \int_1^2 \gamma(\mathbf{r}) = \int_1^2 \left(\nabla \chi(\mathbf{r}) - \frac{2\pi}{\phi_0} \mathbf{A} \right) \cdot d\mathbf{l} \quad (2.72)$$

$$= \chi_2 - \chi_1 - \frac{2\pi}{\phi_0} \mathbf{A} \cdot d\mathbf{l} \quad (2.73)$$

$$= \chi - \frac{2\pi}{\phi_0} BLy \quad (2.74)$$

This leads to the current density

$$J_s = J_c \sin \left(\chi - \frac{2\pi}{\phi_0} BLy \right) = J_c \sin \left(\chi - \frac{2\pi\phi}{W\phi_0} y \right) \quad (2.75)$$

Integration over x leads to

$$\int dy J(y) = \int_0^W J_c \sin \left(\chi - \frac{2\pi}{\phi_0} BLy \right) = J_c \frac{W\phi_0}{2\pi\phi} (\cos(\chi_0) - \cos(2\pi\phi/\phi_0 + \chi_0)) \quad (2.76)$$

Maximising the above equation with respect to χ gives the critical current

$$I_c = W J_c \left| \frac{\sin(\pi\phi/\phi_0)}{\pi\phi/\phi_0} \right| \quad (2.77)$$

2.5 Graphene And Superconductivity: Specular Andreev Reflection

An unusual form of Andreev reflection has been found at graphene - superconductor interfaces [16]. The previously discussed Andreev reflection changes the direction of the incoming particle such that the reflected particle travels on approximately the same trajectory as the incoming one (see section 2.2). This process is called Andreev retro reflection and is illustrated in figure 2.4 b. It is only an approximation, because due to its condensation into a cooper pair, the particle will lose energy during the reflection process. In most metals, hardly any energy loss is observed because the Fermi energy of most metals is large compared to the superconducting energy gap, $E_F \gg \Delta$ [17]. Graphene, however, is a semi-metal with low E_F , where the regime with $E_F < \Delta$ is achievable. As a consequence, the E_F dependence of Andreev reflection can be studied in graphene.

The single-particle Hamiltonian for graphene is the Dirac Hamiltonian

$$H = \begin{pmatrix} H_+ & 0 \\ 0 & H_- \end{pmatrix}, \quad (2.78)$$

where

$$H_{\pm} = i\hbar \left(\sigma_x \delta_x \pm \sigma_y \delta_y \right) + U. \quad (2.79)$$

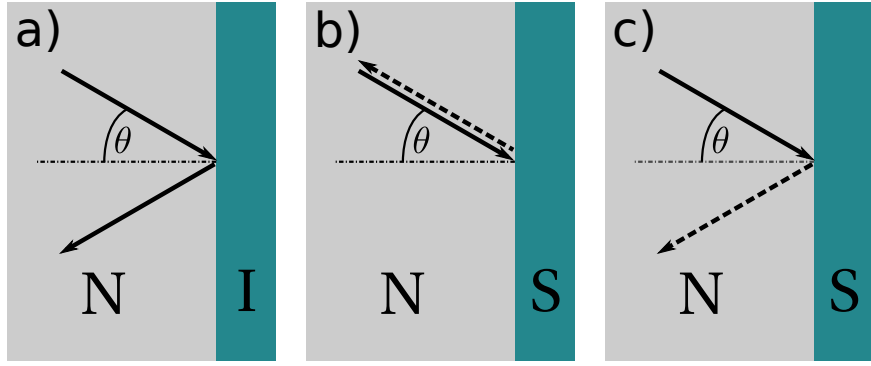


Figure 2.4: Reflection processes. Solid arrows represent electrons, dashed arrows represent holes.
 a) Specular reflection of an electron at an insulating interface (I).
 b) Andreev retro reflection of an electron with into a hole.
 c) Specular Andreev reflection of an electron into an hole with incident angle $\theta \neq 0$.

For the expression of H_{\pm} , the pauli matrices σ_i have been used. An electrostatic potential, $U(\mathbf{r})$, can be present in the sample. Here, it is chosen such that

$$U(\mathbf{r}) = -U_0\theta(x) \quad (2.80)$$

This modifies the BdG equation, resulting in

$$\begin{pmatrix} H_{\pm} + E_F & \Delta \\ \Delta^* & E_F - H_{\pm} \end{pmatrix} \begin{pmatrix} u \\ v \end{pmatrix} = \epsilon \begin{pmatrix} u \\ v \end{pmatrix}, \quad (2.81)$$

where the electron spinor has two components $(u_1, u_2) = (\Psi_{A+}, \Psi_{B+})$, and the hole spinor is $(v_1, v_2) = (\Psi_{A-}^*, \Psi_{B-}^*)$. Eq. (2.81) leads to the energy spectrum

$$\epsilon = \sqrt{|\Delta|^2 + (E_F - U \pm \hbar v |\mathbf{k}|)^2}, \quad (2.82)$$

with

$$|\mathbf{k}| = \sqrt{k_x^2 + k_y^2}. \quad (2.83)$$

The dispersion relation has four solutions for \mathbf{k} . Two of them lead to a positive velocity $v_x = \hbar^{-1} d\epsilon/dk_x$ corresponding to each one electronic and one hole excitation. A reflected hole can be in one of the following two states: It is reflected either into the conduction band with $\epsilon < E_F$ (retro reflection) or into the valence band with $\epsilon > E_F$ (specular reflection). Specular reflection is the dominating process, when the Fermi energy is smaller than the gap energy, $E_F \ll \Delta$. For $E_F \gg \Delta$, the retro reflection dominates.

3 A Framework For The Numerical Analysis

3.1 Tight Binding Model For Graphene

Tight binding models are simple, yet powerful methods to calculate the electronic band structure of a system consisting of many lattice sites. Each lattice site is represented in the Hamiltonian as an atomic potential. The basic premise is that the solution to the Schrödinger equation of the isolated system, an electron at a specific site in an atomic potential, is known. The wave function of this electron interacting with the whole lattice (interacting with all other atomic potentials from the other lattice sites) can be constructed from the overlap of the atomic wave functions. Following the notation in [18] and also from [19], the atomic orbital is denoted with ϕ_m . This is the orbital of an atom for unit cell index m , where $m = 1, \dots, M$. From these orbitals ϕ_m , a Bloch state Φ_m is constructed. This Bloch state then represents the lattice symmetry (vertauscht mit dem Translationsoperator).

$$\Phi_m(\mathbf{k}, \mathbf{r}) = \frac{1}{\sqrt{N}} \sum_{i=1}^N e^{i\mathbf{k}\mathbf{R}_{m,i}} \phi_m(\mathbf{r} - \mathbf{R}_{m,i}) \quad (3.1)$$

$\Phi_m(\mathbf{k}, \mathbf{r})$ is the Bloch state, the index i labels the unit cell, with $i = 1, \dots, N$ (for each unit cell there are M orbitals). $\mathbf{R}_{m,i}$ is the position vector of orbital m in unit cell i . Using this new state, the electronic wave function can be expressed as a linear combination of these orbitals

$$\Psi_j(\mathbf{k}, \mathbf{r}) = \sum_{m=1}^M \psi_{j,m}(\mathbf{k}) \Phi_m(\mathbf{k}, \mathbf{r}) \quad (3.2)$$

with coefficients $\psi_{j,m}$. The energy of the Hamiltonian \mathcal{H} is given by

$$E_j(\mathbf{k}) = \frac{\langle \Psi_j | \mathcal{H} | \Psi_j \rangle}{\langle \Psi_j | \Psi_j \rangle} \quad (3.3)$$

the coefficients can be found by minimising E_j . Introducing the transfer integral matrix H and the overlap integral matrix S , one can write

$$H\psi_j = E_j S_j \psi_j \quad (3.4)$$

The coefficients of the transfer matrix and the overlap matrix are given by

$$H_{m,m'} = \langle \Phi_m | \mathcal{H} | \Phi_{m'} \rangle \quad (3.5)$$

$$S_{m,m'} = \langle \Phi_m | \Phi_{m'} \rangle \quad (3.6)$$

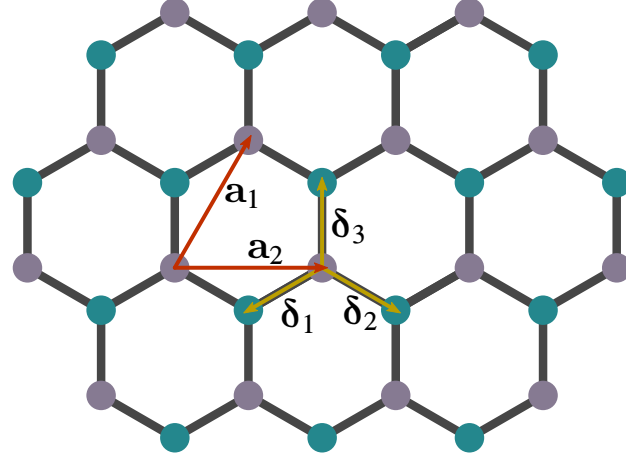


Figure 3.1: Monolayer graphene lattice with lattice vectors \mathbf{a}_1 , \mathbf{a}_2 for sublattice A. The vectors δ_i give the shift to the atoms of sublattice B.

So, in order to find the band energies E_j , these coefficients $H_{m,m'}$ and $S_{m,m'}$ need to be determined. Once they have been calculated, the energies can be found by solving

$$\det [H - E_j S] = 0 \quad (3.7)$$

3.1.1 Monolayer Graphene

Let us apply the introduced procedure to monolayer graphene. Graphene has two atoms per unit cell and one $2p_z$ orbital per atom is taken into account. Graphene has two sets of lattice vectors, \mathbf{a}_1 , \mathbf{a}_2 and \mathbf{b}_1 , \mathbf{b}_2 , depending on which the lattice site (see figure XY). The sublattices are labelled A and B. The atomic orbitals are therefore also labelled with a sublattice index, ϕ_A and ϕ_B . The transfer matrix H is

$$H = \begin{pmatrix} \phi_A^* \mathcal{H} \phi_A & \phi_A^* \mathcal{H} \phi_B \\ \phi_B^* \mathcal{H} \phi_A & \phi_B^* \mathcal{H} \phi_B \end{pmatrix} \quad (3.8)$$

$$\equiv \begin{pmatrix} H_{AA} & H_{AB} \\ H_{BA} & H_{BB} \end{pmatrix} \quad (3.9)$$

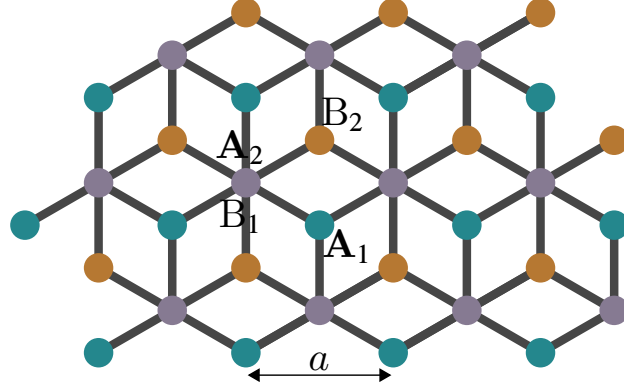
For the diagonal elements, H_{AA} and H_{BB} , the strongest contribution comes from the interaction of the orbital with itself. The hopping from one A site to another A site is significantly smaller and is therefore neglected. (Makes sense, since the nearest neighbours of an A site are B sites).

$$H_{AA} \approx \frac{1}{N} \sum_{i=1}^N \langle \phi_A(\mathbf{r} - \mathbf{R}_{A,i}) | \mathcal{H} | \phi_A(\mathbf{r} - \mathbf{R}_{A,i}) \rangle \equiv \epsilon_A \quad (3.10)$$

$H_{BB} = \epsilon_B$ holds in the analogous way. Since graphene has two identical sublattices A and B, the on-diagonal energies are equal: $\epsilon_A = \epsilon_B$. Off diagonal elements H_{AB} and H_{BA} describe the possibility of hopping from one sublattice to the other.

$$H_{AB} \approx \frac{1}{N} \sum_{i=1}^N \sum_{l=1}^3 e^{i\mathbf{k}\delta_l} \langle \Phi_A(\mathbf{r} - \mathbf{R}_{A,i}) | \mathcal{H} | \Phi_B(\mathbf{r} - \mathbf{R}_{A,i} - \delta_l) \rangle \quad (3.11)$$

$$\equiv -\gamma_0 f(\mathbf{k}), \quad (3.12)$$



where

$$\gamma_0 = -\langle \Phi_A(\mathbf{r} - \mathbf{R}_{A,i}) | \mathcal{H} | \Phi_B(\mathbf{r} - \mathbf{R}_{B,i} - \boldsymbol{\delta}_l) \rangle \quad (3.13)$$

$$f(\mathbf{k}) = \sum_{l=1}^3 e^{i\mathbf{k}\boldsymbol{\delta}_l} \quad (3.14)$$

$\boldsymbol{\delta}_l$ gives the distance vectors from one given A atom to another B site. The other off-diagonal element of H is $H_{BA} = H_{AB}^* = -\gamma_0 f^*(\mathbf{k})$. The overlap matrix elements on the diagonal, S_{AA} and S_{BB} equal to one, since

$$S_{AA} = S_{BB} = \langle \Phi_A(\mathbf{r} - \mathbf{R}_{j,i}) | \Phi_A(\mathbf{r} - \mathbf{R}_{j,i}) \rangle = 1. \quad (3.15)$$

For the off-diagonal elements, similar to eq. (3.12), a coefficient s_0 is introduced.

$$S_{AB} = S_{BA} = s_0 f(\mathbf{k}) \quad (3.16)$$

$$s_0 = \langle \Phi_A(\mathbf{r} - \mathbf{R}_{A,i}) | \Phi_B(\mathbf{r} - \mathbf{R}_{B,l}) \rangle \quad (3.17)$$

Finalizing, the Hamiltonian H and the overlap integral matrix S are

$$H = \begin{pmatrix} \epsilon_1 & -\gamma_0 f(\mathbf{k}) \\ -\gamma_0 f^*(\mathbf{k}) & \epsilon_B \end{pmatrix} \quad (3.18)$$

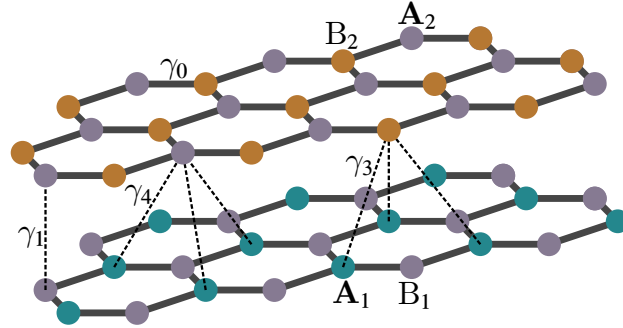
$$S = \begin{pmatrix} 1 & s_0 f(\mathbf{k}) \\ s_0 f^*(\mathbf{k}) & 1 \end{pmatrix} \quad (3.19)$$

The energy γ_0 and the coefficient s_0 have been determined experimentally [20]: $\gamma_0 = 3.033\text{eV}$ and $s_0 = 0.129$.

3.1.2 Bilayer Graphene

Bilayer graphene consists of two layers of graphene, and each of these layers has two sublattices. A lattice site in bilayer graphene can there be in one of the four sublattices A_1 , B_1 , A_2 and B_2 , where the integer 1, 2 labels the layer. Using the notation of the SWM model, [21], [22], the transfer matrix can be written as

$$H = \begin{pmatrix} \epsilon_{A_1} & -\gamma_0 f(\mathbf{k}) & \gamma_4 f(\mathbf{k}) & -\gamma_3 f^*(\mathbf{k}) \\ -\gamma_0 f^*(\mathbf{k}) & \epsilon_{B_1} & \gamma_1 & \gamma_4 f(\mathbf{k}) \\ \gamma_4 f^*(\mathbf{k}) & \gamma_1 & \epsilon_{A_2} & -\gamma_0 f(\mathbf{k}) \\ -\gamma_3 f(\mathbf{k}) & \gamma_4 f^*(\mathbf{k}) & -\gamma_0 f^*(\mathbf{k}) & \epsilon_{B_2} \end{pmatrix} \quad (3.20)$$



The basis of this matrix is $(|\phi_{A_1}\rangle, |\phi_{B_1}\rangle, |\phi_{A_2}\rangle, |\phi_{B_2}\rangle)$ and therefore describes an AB -stacked bilayer system. If the representation of eq (3.20) had the basis $(|\phi_{B_1}\rangle, |\phi_{A_1}\rangle, |\phi_{A_2}\rangle, |\phi_{B_2}\rangle)$, the matrix would describe an AA -stacked bilayer system. In an AB (AA) stacked system, an A_2 atom would be directly above an atom of the B_1 (A_1) sublattice. In the most general case, the energies ϵ on the diagonal are not equal. The off-diagonal parameters γ are given by

$$\gamma_0 = -\langle \phi_{A_1} | \mathcal{H} | \phi_{B_1} \rangle = -\langle \phi_{A_2} | \mathcal{H} | \phi_{B_2} \rangle, \quad (3.21)$$

$$\gamma_1 = \langle \phi_{A_2} | \mathcal{H} | \phi_{B_1} \rangle, \quad (3.22)$$

$$\gamma_3 = -\langle \phi_{A_1} | \mathcal{H} | \phi_{B_2} \rangle, \quad (3.23)$$

$$\gamma_4 = \langle \phi_{A_1} | \mathcal{H} | \phi_{A_2} \rangle = \langle \phi_{B_1} | \mathcal{H} | \phi_{B_2} \rangle \quad (3.24)$$

The γ_0 parameter describes nearest neighbour hopping within a layer (in-plane hopping) and does therefore contain the factor $f(\mathbf{k})$, which is defined as the distance to the surrounding neighbours in one layer. Interlayer hopping between A_2 and B_1 atoms is included with the parameter γ_1 . This hopping is vertical from one layer to the other. The parameters γ_3 and γ_4 also describe interlayer hopping, but this hopping is not vertical (it does not connect lattice sites that are directly in line). It can be thought of as a combination of in-plane hopping followed by vertical hopping (see figure). The overlap matrix of bilayer graphene can be introduced with the parameters $s_0 = \langle \Phi_{A_1} | \Phi_{B_1} \rangle = \langle \Phi_{A_2} | \Phi_{B_2} \rangle$ and $s_1 = \langle \Phi_{A_2} | \Phi_{B_1} \rangle$ [23]. The parameters s_3 and s_4 are neglected, because they are small (why?).

$$S = \begin{pmatrix} 1 & s_0 f(\mathbf{k}) & 0 & 0 \\ s_0 f^*(\mathbf{k}) & 1 & s_1 & 0 \\ 0 & s_1 & 1 & s_0 f(\mathbf{k}) \\ 0 & 0 & s_0 f^*(\mathbf{k}) & 1 \end{pmatrix} \quad (3.25)$$

The overlap matrix S is often approximated as a unit matrix and the parameters s_0 and s_1 are neglected. These parameters s_0 and s_1 describe the non-orthogonality of orbitals, which is small for energies $E \leq \gamma_1$.

The tight binding parameters can be determined experimentally using Raman scattering [24] or infrared spectroscopy [25]. The values determined in [25] are

$$\gamma_0 = 3.16, \gamma_1 = 0.381, \gamma_3 = 0.38, \gamma_4 = 0.14. \quad (3.26)$$

3.1.3 Tight Binding Models And `kwant`

The numerical calculations in this thesis were performed using `kwant` [26], an open source Python package for calculations with tight binding models. For implementing the system in `kwant`, the tight binding model has to be defined. This means, a lattice with corresponding symmetry has to

be build and the hoppings between the lattice points have to be defined. The bilayer system that is used in this thesis is *AB*-stacked and the presence of a magnetic field is considered, entering the Hamiltonian with the Peierls approximation:

$$\phi_{i,j} = \frac{e}{\hbar} \int_i^j \mathbf{A} d\mathbf{r}. \quad (3.27)$$

The tight binding Hamiltonian reads

$$H = -\gamma_0 \sum_{i,j} e^{i\phi_{i,j}} a_{m,i}^\dagger b_{m,i} - \gamma_1 \sum_j a_{1,j}^\dagger b_{2,j} - \sum_{i,m} (\mu_i - (-1)^m \delta_i) (a_{m,i}^\dagger a_{m,i} + b_{m,i}^\dagger b_{m,i}). \quad (3.28)$$

The different layers of BLG are indexed with $m = 1, 2$. The operators $a_{m,i}^\dagger$, $a_{m,i}$ create and annihilate an electron of sublattice *A* on layer m at site i . In the same way, $b_{m,i}^\dagger$, $b_{m,i}$ are the creation and annihilation operators for the sublattice *B*. The onsite energies are

$$\epsilon_{A_1} = \epsilon_{B_1} = \mu_i + \delta_i \quad (3.29)$$

$$\epsilon_{A_2} = \epsilon_{B_2} = \mu_i - \delta_i \quad (3.30)$$

$$(3.31)$$

Here, μ and δ are defined as

$$\mu_i = \frac{\varphi_{BG} + u_i \varphi_{SG}}{2} \quad (3.32)$$

$$\delta_i = \frac{\varphi_{BG} - u_i \varphi_{SG}}{\eta} \quad (3.33)$$

u_i is used as a parameter that defines, if the lattice site i is within a gated region ($u_i = 1$) (underneath a topgate) or not ($u_i = 0$).

3.2 Random Matrix Theory Tor Transport

3.2.1 Fundamental Idea

To describe the transport through a conducting region of interest, which is in between of two ideal leads. Ideal leads means that there is no disorder present, whereas the conductor is a disordered system. The question that the random matrix theory is answering, is: how can one describe the transport from one lead, through the disordered region to the other lead? Essential for this transport theory is the work of Landauer (cite!), who described ballistic transport through a 1D channel as a transmission problem.

The transport through the conducting region can be written in terms of an incident wave c^{in} and a reflected/transmitted wave c^{out} . The scattering matrix \mathcal{S} relates the amplitudes of these wave functions.

$$c^{\text{out}} = \mathcal{S} c^{\text{in}}, \quad (3.34)$$

where

$$c^{\text{in}} = (a_1^+, a_2^+, \dots, a_N^+, b_1^+, b_2^+, \dots, b_N^+) \quad (3.35)$$

$$c^{\text{out}} = (a_1^-, a_2^-, \dots, a_N^-, b_1^-, b_2^-, \dots, b_N^-) \quad (3.36)$$

The coefficients a represent the left lead and b the right lead. The \pm sign indicates, if it describes a right or left moving electron (see figure). The integer $n = 1, 2, \dots, N$ is the index for the propagating

modes. In this case, there are N modes in both the left and the right lead. The scattering matrix has the form

$$\mathcal{S} = \begin{pmatrix} r & t' \\ t & r' \end{pmatrix} \quad (3.37)$$

where r, r' are reflection matrices, and t, t' are $N \times N$ transmission matrices. Both the transmission and the reflection matrices have the dimension $N \times N$. The scattering matrix is unitarity, since the current is conserved:

$$\mathcal{S}^{-1} = \mathcal{S}^\dagger. \quad (3.38)$$

Consequently, the matrices $tt^\dagger, t't^\dagger, 1 - rr^\dagger$ and $1 - r'r^\dagger$ have the same set of eigenvalues T_1, T_2, \dots, T_N , each of them being a real number between 0 and 1.

It is useful to write the scattering matrix \mathcal{S} in terms of the transmission eigenvalues T_n , introducing the matrix $\mathcal{T} = \text{diag}(T_1, T_2, \dots, T_n)$. Each of the eigenvalues of \mathcal{T} is a real value between 0 and 1. This rewriting is done in [27] and is called polar decomposition

$$\mathcal{S} = \begin{pmatrix} U & 0 \\ 0 & V \end{pmatrix} \begin{pmatrix} -\sqrt{1-\mathcal{T}} & \sqrt{\mathcal{T}} \\ \sqrt{\mathcal{T}} & \sqrt{1-\mathcal{T}} \end{pmatrix} \begin{pmatrix} U' & 0 \\ 0 & V' \end{pmatrix} \quad (3.39)$$

U, V are $N \times N$ unitary matrices.

The scattering matrix relates incoming (c^{in}) states to outgoing (c^{out}) states. It is also possible to look at the transfer matrix M , which relates states from the left lead (c^{left}) to states in the right lead (c^{right}):

$$c^{\text{right}} = M c^{\text{left}} \quad (3.40)$$

where

$$c^{\text{left}} = (a_1^+, a_2^+, \dots, a_N^+, a_1^-, a_2^-, \dots, a_N^-) \quad (3.41)$$

$$c^{\text{right}} = (b_1^+, b_2^+, \dots, b_N^+, b_1^-, b_2^-, \dots, b_N^-) \quad (3.42)$$

$$M = \begin{pmatrix} V & 0 \\ 0 & V'^\dagger \end{pmatrix} \begin{pmatrix} \sqrt{\mathcal{T}^{-1}} & \sqrt{\mathcal{T}^{-1}-1} \\ \sqrt{\mathcal{T}^{-1}-1} & \sqrt{\mathcal{T}^{-1}} \end{pmatrix} \begin{pmatrix} U' & 0 \\ 0 & U^\dagger \end{pmatrix} \quad (3.43)$$

Both the transfer matrix M and the scattering matrix S describe the conductive region. The nice feature of the transfer matrix can be seen, if multiple disordered regions, each separated by ideal leads, are considered. The transfer matrix of the whole system is a multiplication of each regions individual transfer matrix. (which is an advantage, the scattering matrix stuff is then a bit of a fuck off...) The conductance of such a disordered region is given by the sum of the transmission eigenvalues T_n :

$$G = G_0 \sum_{n=1}^N T_n, \quad G_0 = \frac{2e^2}{h} \quad (3.44)$$

This is cool. But there is not much context...

3.2.2 Supercurrent In An SNS Junction

Considering an SNS junction. The wave functions for an incident wave and an reflected/transmitted wave contain now coefficients for electrons and holes:

$$c_N^{\text{in}} = (c_e^+(N_1), c_e^-(N_2), c_h^-(N_1), c_h^+(N_2)) \quad (3.45)$$

$$c_N^{\text{out}} = (c_e^-(N_1), c_e^+(N_2), c_h^-(N_1), c_h^+(N_2)) \quad (3.46)$$

N_1 is the number of modes in the left lead, N_2 is the number of modes in the right lead. In the special case of scattering between a normal conductive region and a superconductor, two types of scattering have to be distinguished. For one, there is the normal scattering of electrons and there is Andreev reflection of electrons at the superconductor. The scattering process at the normal region is described by the normal scattering matrix s_N , that connects an incident wave with a reflected/transmitted one.

$$c_N^{\text{out}} = s_N(\epsilon) c_N^{\text{in}} \quad (3.47)$$

This scattering matrix s_N is

$$s_N(\epsilon) = \begin{pmatrix} s_0(\epsilon) & 0 \\ 0 & s_0(\epsilon) \end{pmatrix}, \quad (3.48)$$

where

$$s_0 = \begin{pmatrix} r_{11} & t_{12} \\ t_{21} & r_{22} \end{pmatrix} \quad (3.49)$$

The Andreev reflection process is described by another scattering matrix, the Andreev scattering matrix s_A . For energies $\epsilon < \Delta$, there are no propagating modes inside the superconductor. And for $\Delta_0 \ll E_F$, the normal reflection at the NS interface can be ignored and only Andreev scattering is taken into account.

$$s_A = \alpha(\epsilon) \begin{pmatrix} 0 & r_A \\ r_A^* & 0 \end{pmatrix}, \quad (3.50)$$

with $\alpha(\epsilon) = \exp\left(-i \arccos \frac{\epsilon}{\Delta}\right)$

$$r_A = \begin{pmatrix} e^{i\phi/2} \mathbb{1} & 0 \\ 0 & e^{-i\phi/2} \mathbb{1} \end{pmatrix} \quad (3.51)$$

From the structure of the Andreev scattering matrix, it can be seen that an electron mode is transformed into a hole mode, while the mode index n does not change. This transformation is accompanied by a phase shift of $-\arccos \frac{\epsilon}{\Delta}$, which comes from the decay into the superconducting region. Also, a phase of $\phi/2$ ($-\phi/2$), where ϕ is the superconducting phase difference, is added for reflection from electron to hole (hole to electron).

A bound state in the SNS junction forms, when

$$c_{\text{in}} = s_A(\epsilon) s_N(\epsilon) c_{\text{in}} \quad (3.52)$$

holds. In the short junction limit, $L \ll \xi$, it holds that

$$s_0(\epsilon) \approx s_0(-\epsilon) \approx s_0(0) \equiv s_0 \quad (3.53)$$

This can be used to simplify the normal scattering matrix $s_N(\epsilon)$ equation (3.48). Using this approximation, the bound state condition eq. (3.52) becomes

$$\begin{pmatrix} s_0^\dagger & 0 \\ 0 & s_0^T \end{pmatrix} \begin{pmatrix} 0 & r_A^* \\ r_A & 0 \end{pmatrix} c_{\text{in}} = \exp\left(i \arccos \frac{\epsilon}{\Delta}\right) c_{\text{in}} \quad (3.54)$$

This can be simplified further. By applying a Joukowsky transformation, it is possible to write

$$\begin{pmatrix} 0 & -iA \\ iA & 0 \end{pmatrix} c_{\text{in}} = \frac{\epsilon}{\Delta} \quad (3.55)$$

with $A = \frac{1}{2}(r_A s_0 - s_0^T r_A)$. This leads to

$$A^\dagger A c_{\text{in}} = \frac{\epsilon^2}{\Delta^2} c_{\text{in}} \quad (3.56)$$

So far, the condition for an Andreev bound state has been simplified according to the short junction approach. To get an expression for the current, the free energy F is needed [28]:

$$I = \frac{2e}{\hbar} \frac{dF}{d\phi} \quad (3.57)$$

the free energy F has been calculated as [29]

$$F = -2k_B T \sum_{\epsilon > 0} \ln \left[2 \cosh \frac{\epsilon}{2k_B T} \right] + \dots \quad (3.58)$$

which is the free energy of a non interacting electron. So the current is

$$I = -\frac{2e}{\hbar} \sum_p \tanh \left(\frac{\epsilon_p}{2k_B T} \right) \frac{d\epsilon_p}{d\phi} \quad (3.59)$$

The derivation of the energy with respect to the phase can be obtained from eq. (3.56).

$$\frac{d\epsilon}{d\phi} = \frac{\Delta^2}{2\epsilon} \frac{\langle c_{\text{in}} | \frac{d(A^\dagger A)}{d\phi} | c_{\text{in}} \rangle}{\langle c_{\text{in}} | c_{\text{in}} \rangle} \quad (3.60)$$

4

Experimental Motivation

4.1 Introduction

Can the supercurrent be monitored in a bilayer graphene (BLG) sample? The experimental work underpinning this thesis concerns itself with this question. In a conventional tunnel barrier, the supercurrent can only be tuned when the sample geometry or the environment temperature is changed. Moreover, the tunnel barrier should not exceed a certain width in order to make the supercurrent observable. The central idea of the particular set-up presented here is to create a weak link in the form of a quantum point contact (QPC). A weak link is a conductive material in which superconductivity can be induced because of the superconducting proximity effect [30]. The key achievement of this work is showing that with this QPC geometry, the supercurrent can be controlled both in its amplitude as well as in the spatial distribution within the set-up, which has not been observed so far. Figure 4.1 shows a schematic of the set-up. The BLG layer (black)

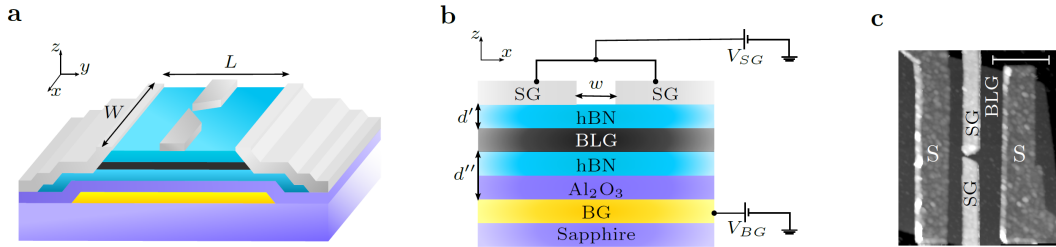


Figure 4.1: A schematic of the device. The top view **a** displays the two fingers of the QPC topgate in the middle of the device. The cross-sectional schematic **b** shows the superconducting material Al_2O_3 lying on top of the back gate. The BLG is encapsulated between two layers of hBN. The split width w is the width between the two fingers of the QPC gate. **c** shows an image of the device, with the scale on the upper right corresponding to $1 \mu\text{m}$. Reprinted from [10].

is of width W and a length L . It is encapsulated between two layers of hexagonal boron nitride (hBN, blue) and lies on top of a back-gate. A top-gate with a split of width w in the middle, as depicted in see figure 4.1 b, covers the the heterostructure. This device layout enables tuning the back-gate potential V_{BG} independently from the top-gate or split-gate potential V_{SG} .

By gating the material with V_{BG} , an overall potential is applied at the whole region, lifting the Fermi energy E_F of the system. At the same time, the region that is covered with the top gate is gated locally by the split-gate potential, while creating a displacement field along the sample. The displacement field breaks the symmetry of the BLG, and the two layers are at different energy levels. As as result, a gap in the BLG spectrum is opened [31].

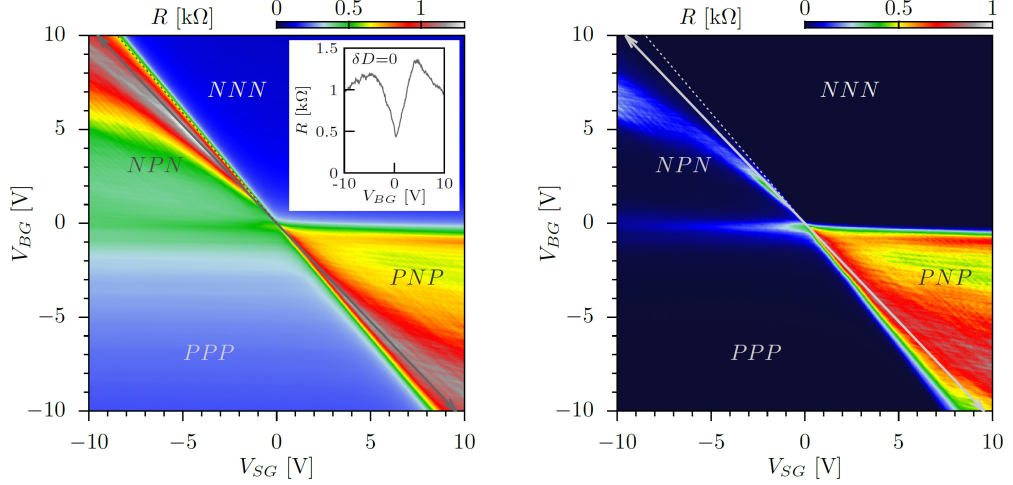


Figure 4.2: Resistance in the sample R in $k\Omega$ depends on the split-gate V_{SG} on the x-axis and back-gate V_{BG} on the y-axis. The left picture displays data of the normal state, the right picture displays data of the superconducting state. The grey arrow indicates the displacement field line, where the fields created by back-gate and split-gate voltage are equal. Reprinted from [10].

4.2 Normal State Analysis

In figure 4.2, the normal state resistance dependence on both back-gate and split-gate voltage is shown. The results of the normal state resistance differ from previous studies [32], [33]. The gate map in 4.2 has the back-gate as y-axis, the split-gate forming the QPC as x-axis, and the color indicates the strength of measured resistance. The diagonal line where the fields created back and split-gate are equal is called displacement field line (indicated with a grey arrow). The four quadrants are named according to how the BLG is gated: The first letter is the doping of the BLG region between the left superconductor and the split-gate, which is not gated. The middle letter indicates the doping underneath the region of the split-gate, and the third letter is the BLG doping between split-gate and right superconducting lead. Depending on the choice of V_{BG} and V_{SG} , the overall doping can be either one of NNN , NPN , PPP , or PNP . In the upper left quadrant, where the region is NPN doped, the maximum resistance seems to follow the displacement field line on the diagonal. After a certain point, however, it bends, and its maximum resistance is not found to be on the diagonal line anymore. This behaviour was not seen in [32], [33] – these studies observed the maximum resistance to be on the diagonal line. The effect can be seen in the normal state resistance map, but it is strongly visible in the superconducting state. The overall resistance of the sample is higher on the p-side, because the superconducting leads are slightly n-doped. This leads to a PN -junction at each contact, which is seen in the gate map for the superconducting state. The PNP -region remains resistive, while the NPN -region shows zero resistance. How can the bending in the resistance peak be explained? Since the charge carrier density in the sample is low ($2.8 \cdot 10^{18} \text{ cm}^{-2}$), the influence of the back gate is important. The higher the back gate value, the less the charge carrier density is affected by the split gate and the stray fields it produces. In the lower NPN -region, the split gates work as intended: The channel region – the region between the split gates where the supercurrent can pass through – is conductive, because the back gate dominates. The BLG directly underneath the gates is P -doped, and the area between the two gate fingers is N -doped. A channel is created, where the current can pass through. This set-up is illustrated in the middle picture of figure 4.3. However, in the region where the resistance curve starts to bend, the stray fields from the split gate dominate. The area underneath the gates is still

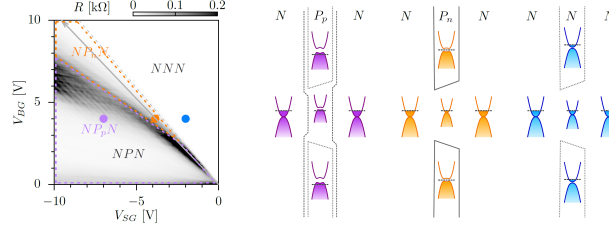


Figure 4.3: A detailed view on the NPN-region of the resistance map. When the split-gate voltage V_{SG} dominates, the area between the two split-gate fingers (the violet framed region) becomes P-doped because of the stray fields of the V_{SG} . When the constriction works as a 1D-channel, the area between the fingers (the orange framed region) is N-doped and the current can pass through this region. In the blue framed region, the sample is overall conductive. Reprinted from [10].

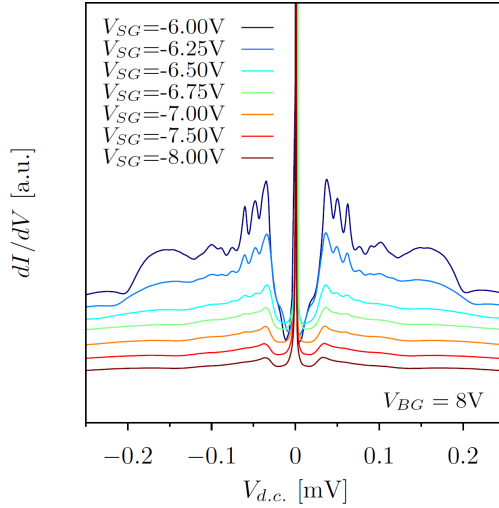


Figure 4.4: Differential conductance versus voltage applied for different values of V_{SG} . The higher the split-gate voltage, the less peaks are visible. Reprinted from [10].

P-doped, but now the area between the fingers is slightly P-doped as well (see the right picture in figure 4.3), which effectively leads to a blocking behaviour of the channel, and eventually to an increased resistance.

4.3 Superconducting State

The superconducting state is analysed in the NPN-region of the gatemap. The confinement of the two-dimensional supercurrent (in the case of no barrier present) to transport on a one-dimensional channel manifests in a Fraunhofer pattern of the supercurrent and in the differential conductance dI/dV . While there is no constriction present, at $V_{SG} = 0V$, multiple Andreev reflections take place. When the constriction – the QPC barrier – forms, the process of multiple Andreev reflections is suppressed, because the probability of an electron reaching the opposite superconducting lead and getting Andreev reflected there is low. This is observable in the differential conductance for different values of the splitgate V_{SG} . Andreev reflection manifests within the dI/dV curve in form of as peaks. In figure 4.4, the dI/dV curves are plotted. For $V_{SG} = 0V$ (blue curve), sharp peaks can be seen. These peaks vanish with increasing split-gate voltage. By probing the magnetic interference pattern, the supercurrent density can be explored. When the junction geometry

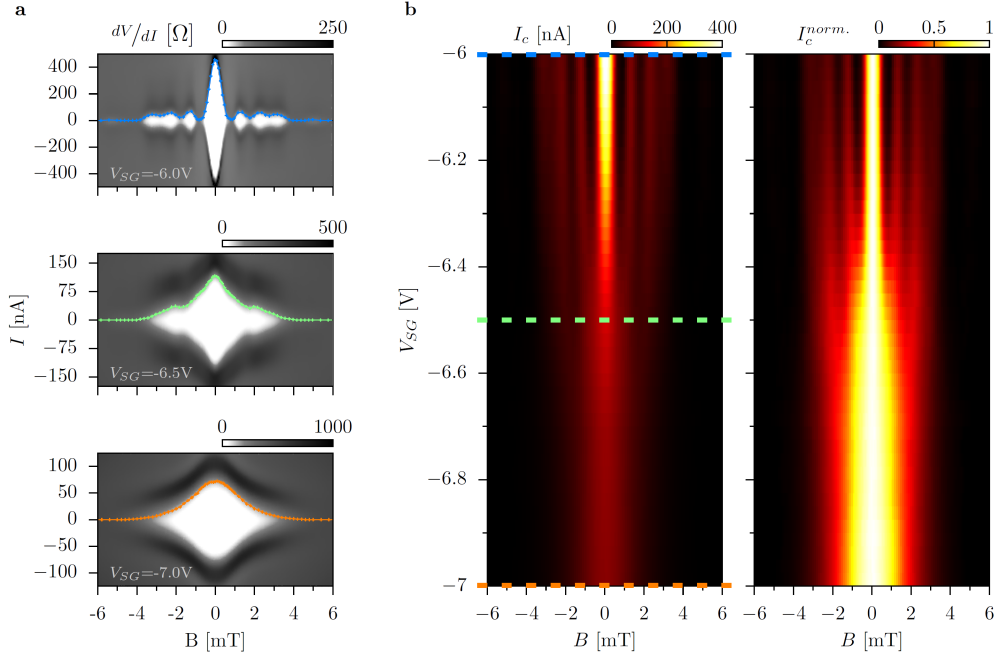


Figure 4.5: **a** shows differential resistance dV/dI plotted against the magnetic field B . The y-axis indicates the strength of the critical current, which is the dotted, coloured line. **b** shows the critical current (left) and normalised critical current (right) versus a magnetic field (x-axis) for different values of V_{SG} . The dotted curves from **a** correspond to different stadiums of the transition from 2D-Fraunhofer pattern to a bell-shaped pattern where the current is confined. Reprinted from [10].

changes, for example because the split-gate voltage is increased and a constriction starts to form, the Fraunhofer pattern will change accordingly. Figure 4.5 b) shows magnetic interferometry measurements at a constant back-gate voltage V_{BG} . The x-axis indicates the magnetic field B and the y-axis is the split-gate voltage V_{SG} . The colour displays the strength of the critical current. The confinement of the current can be seen in the plots in figure 4.5 a), where I_c curves are plotted for $V_{SG} = -6 V$, $-6.5 V$, $-7 V$. For $V_{SG} = -6V$, the observed Fraunhofer pattern indicates a two-dimensional current flow. With increasing V_{SG} , the lobes of the pattern are lifted. When the split-gate reaches $V_{SG} = -7 V$, the constriction has formed, and the Fraunhofer pattern has vanished: A bell-shaped pattern is observed. This shows a transition from the beating to the non-beating, gaussian pattern indicates that a one-dimensional channel has formed. A similar transition from a Fraunhofer pattern to a gaussian-like decay has been observed before, for example in [34], where a long SNS junction has been studied.

5 Analytical Model

5.1 Foundation Of The Quasi-classical Model

From section 2.3 it is known that Andreev reflection of electrons in a SNS junction leads to Andreev bound states within the junction. Each one of these bound states contributes to the total current through the junction. Essentially, a bound state can be expressed as a trajectory from one superconductor through the normal metal to the other superconductor. The superconducting current density is found through geometrical analysis of possible trajectories. The total current density is then found by adding up all these trajectories. The two dimensional junction (schematic

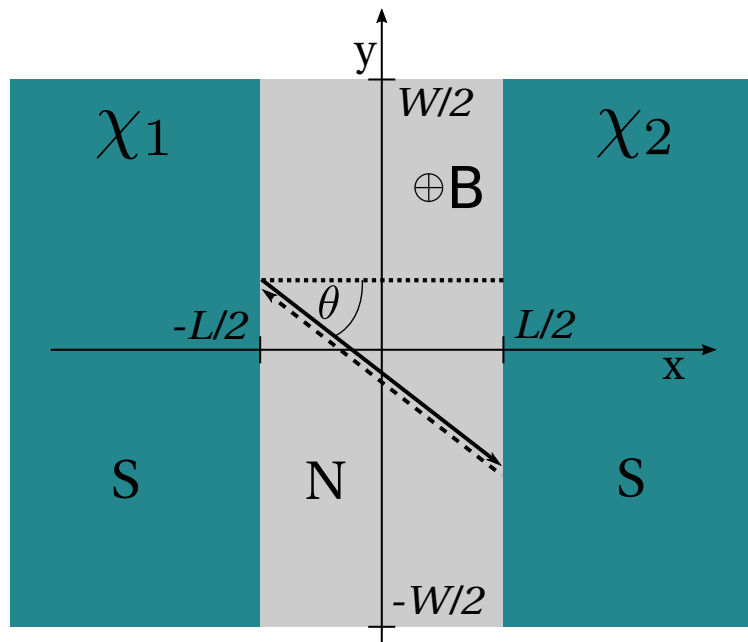


Figure 5.1: An SNS junction with width W and length L . A trajectory connecting the interfaces is parametrized by the angle θ between the trajectory and the x -axis. χ_1 and χ_2 are the superconducting phases, with total phase difference $\chi = \chi_2 - \chi_1$.

shown in fig 5.1) is a short and wide junction with width W and length L , where $W \gg L$. The NS-interfaces are parallel to the y -axis and are placed at $x = \pm L/2$. Each of the superconducting leads has a phase χ_1 and χ_2 , and the overall phase difference is $\chi = \chi_1 - \chi_2$. The superconducting gap parameter Δ is only present in the superconducting leads. Close to the interface, Δ begins to

decay on a length scale of the superconducting coherence length ξ_0 into the normal region. Similar to the procedure in section 2.3, this decay is neglected and a step-like behaviour is assumed for the superconducting gap parameter:

$$\Delta(x) = |\Delta|e^{\chi_1}\Theta(-L/2 - x) + |\Delta|e^{\chi_2}\Theta(x - L/2). \quad (5.1)$$

The thermal length scale of the system assumed to be larger than the sample length:

$$L_T = \hbar v_F/k_B T \gg L. \quad (5.2)$$

The transport through the junction is assumed to be ballistic, resulting in the trajectories being straight and not being altered by scattering in the normal region. However, the presence of the magnetic field in the normal region of the sample will lead to a bending of the trajectories due to the Lorentz force. Depending on the strength of magnetic field B and the Fermi velocity, the radius of this curve is

$$r_B = \frac{mv_F}{eB} \quad (5.3)$$

In order to justify the assumption of straight trajectories, either the magnetic field has to be weak enough, or the Fermi velocity (wavelength) has to be large (short) enough. Then, the cyclotron radius r_B is larger than the sample size L , and straight trajectories are a valid assumption.

5.2 Plane Set-up: Calculation Of The Critical Current

Summing up the contributions leads to the current through the SNS junctions, the Josephson current $J(\chi)$, which is a function of the superconducting phase difference $\chi = \chi_2 - \chi_1$. By maximizing the Josephson current with respect to χ , one finds the critical current I_c .

A trajectory connecting the two superconducting interfaces can be parametrized by the angle θ between the trajectory and the x-axis. For a trajectory from a point $(-L/2, y_1)$ to another at $(+L/2, y_2)$, the angle for the parametrization is

$$\tan \theta = \frac{y_2 - y_1}{L}. \quad (5.4)$$

Figure 5.1 visualizes this parametrization. Several papers outline approaches to this problem ([35], [11]) and are based on the same concept. The Josephson current in [35] has the form

$$J = \frac{2e}{\pi L} \sum_{\kappa} v_{Fx}^{\kappa} \mathcal{J}(\chi), \quad (5.5)$$

where κ is the tangential momentum with $\kappa^2 + \mathbf{k}_x^2 = k_F^2$. v_{Fx} is the projection of v_F on the x-axis

$$v_{Fx} = v_F \cos \theta \quad (5.6)$$

and $\mathcal{J}(\chi)$ is the current density. A similar ansatz to eq. (5.5) is described in [36]:

$$J = \int_{-W/2}^{+W/2} dy \int_{-p_F}^{+p_F} \frac{dp_y}{2\pi} \cos \theta \mathcal{J}(\chi, \phi). \quad (5.7)$$

For a fixed point at the left interface, the current density is integrated over all possible momenta. This integral can be expressed through the endpoints of a trajectory. The integration over p_y can then be replaced by $p_y = p_F \sin \theta \rightarrow dp_y/d\theta = p_F \cos \theta$. The integration over the angle θ can be

substituted by the integration over y_2 , a point at the right interface. The result for the Josephson current reads

$$J(\chi, \phi = 0) = \frac{2ev_F}{\pi\lambda_F L^2} \int \int_{-W/2}^{W/2} dy_1 dy_2 \frac{\mathcal{J}(\chi)}{\left[1 + \left(\frac{y_1 - y_2}{L}\right)^2\right]^2}. \quad (5.8)$$

By maximizing the Josephson current with respect to χ , the critical current can be found as:

$$I_c(\phi) = \max_\chi \{J(\chi, \phi)\}. \quad (5.9)$$

The current density \mathcal{J} depends on the ratio of W and L . For $W \gg L$, the junction is a short junction, while for $W \ll L$, it is a long junction. In the short junction limit, the current density is calculated in [29]

$$\mathcal{J}^s(\chi) = \frac{\mathcal{T}_n \sin \chi}{\sqrt{1 - \mathcal{T}_n \sin^2 \frac{\chi}{2}}} \quad (5.10)$$

which can be derived in the framework of the scattering matrix formalism. \mathcal{T}_n is the transmission coefficient for a given conducting channel. For low transmission, $\mathcal{T} \ll 1$, only the first addend contributes, which leads to the conventional Josephson relation $J \simeq \mathcal{T} \sin \chi$.

For the long junction, from [11] the following expression can be found:

$$\mathcal{J}^l(\chi) = \sum_{k=1}^{\infty} \frac{(-1)^{k+1} \mathcal{T}^k}{k} \sin(k\chi). \quad (5.11)$$

The coefficient \mathcal{T} has been included phenomenologically in this formula and includes the normal scattering in the sample. Figure 5.2 shows a plot of both short and long junction limit current densities. For $\mathcal{T} \ll 1$, \mathcal{J}^s takes a sinusoidal form, which also true for the long junction limit. For each of those, the classical Josephson relation can be found in the limit of low transmissions:

$$\mathcal{J} \simeq \mathcal{T} \sin \chi \quad (5.12)$$

The current densities differ for a large transmission coefficient $\mathcal{T} \simeq 1$: A sawtooth-like shape is observed in the long junction limit, and in the short junction limit, a sinusoidal shape appears.

Including Magnetic Field

Up to this point, the current has been derived for zero magnetic field. If a finite magnetic field is considered, the phase χ is modified because of two effects: First, the magnetic phase that will be acquired along a trajectory connecting two points y_1 and y_2 leads to an additional term in the phase. Also, the superconducting phases at each interface become functions of $y_{1/2}$ (see [36]):

$$\chi_{1/2} = \mp \frac{1}{2} \left(\chi - \frac{2\pi BL}{\phi_0} y_{1/2} \right) \quad (5.13)$$

$$\tilde{\chi}(y_1, y_2) = \chi_2 - \chi_1 \quad (5.14)$$

$$= \chi - \frac{\pi BL}{\phi_0} (y_1 + y_2) \quad (5.15)$$

Assuming that the London penetration depth is small to zero in the superconducting regions, the following gauge for the vector potential can be used:

$$\mathbf{A} = A_y \mathbf{e}_y, \quad A_y = \begin{cases} -Bx, & -L/2 \leq x \leq L/2, \\ -\frac{1}{2}BL|x|, & |x| > L/2 \end{cases} \quad (5.16)$$

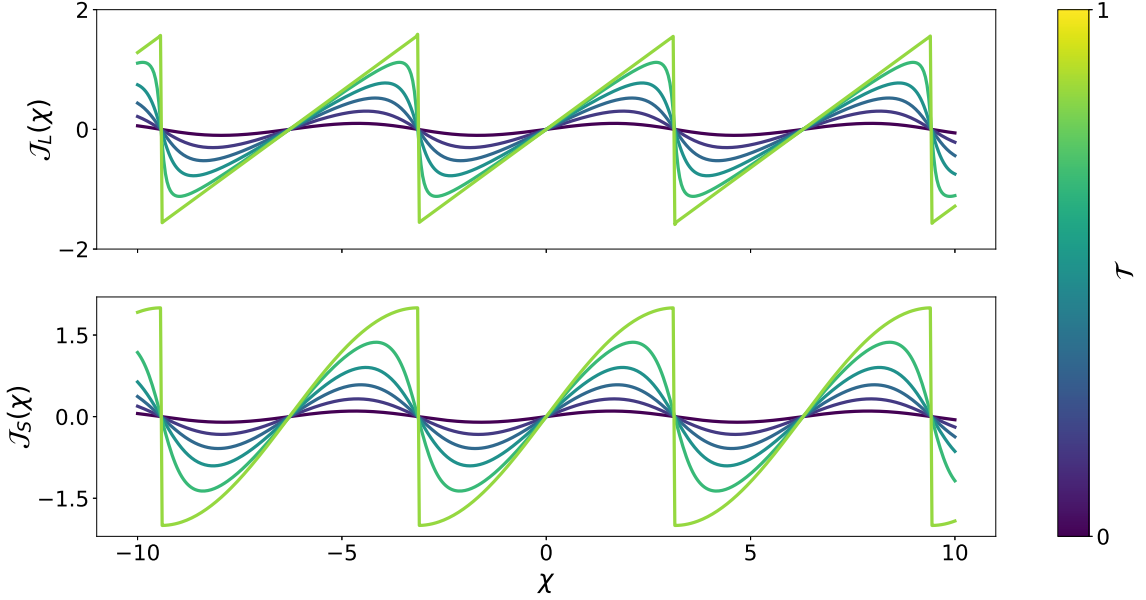


Figure 5.2: Current density plotted against the superconducting phase difference $\chi = \chi_2 - \chi_1$. The density from eq. (5.11) gives the sawtooth like shape for \mathcal{J}^l for high values of \mathcal{T} . In the short junction limit, \mathcal{J}^s holds from eq. (5.10). For low values of the transmission coefficient \mathcal{T} , both current densities have a similar sinusoidal form.

This gauge will give no additional contribution to the phase on straight trajectories

$$\delta\chi = \frac{2\pi}{\Phi_0} \int dl \cdot \mathbf{A} \quad (5.17)$$

$$= \frac{2\pi}{\Phi_0} \int_{-L/2}^{L/2} \frac{dx}{\cos \theta} A_y(x) \sin \theta \quad (5.18)$$

$$= -\frac{2\pi B}{\Phi_0} \frac{y_2 - y_1}{L} \int_{-L/2}^{L/2} x dx \quad (5.19)$$

$$= 0, \quad (5.20)$$

where eq. (5.4) has been used. The total phase for this setup is therefore eq. (5.15). This results in the current phase relation in the expression for the Josephson current from eq. (5.8) to be replaced by the effective phase $\chi \rightarrow \tilde{\chi}(y_1, y_2)$:

$$J(\chi, \phi) = \frac{2ev_F}{\pi\lambda_F L^2} \int \int_{-W/2}^{W/2} dy_1 dy_2 \frac{\mathcal{J}(\tilde{\chi}(y_1, y_2))}{\left[1 + \left(\frac{y_1 - y_2}{L}\right)^2\right]^2} \quad (5.21)$$

Here, the expression for the supercurrent density in the long junction limit and in the limit of low transmission, eq. (5.12) is used. Plugging in the effective phase from eq. (5.15), the Josephson current reads

$$J(\tilde{\chi}(y_1, y_2), \phi) = \mathcal{T} \sin \chi \frac{2ev_F}{\pi\lambda_F L^2} \int \int_{-W/2}^{W/2} dy_1 dy_2 \frac{\cos\left(\frac{\pi\phi}{W}(y_1 + y_2)\right)}{\left[1 + \left(\frac{y_1 - y_2}{L}\right)^2\right]^2}, \quad (5.22)$$

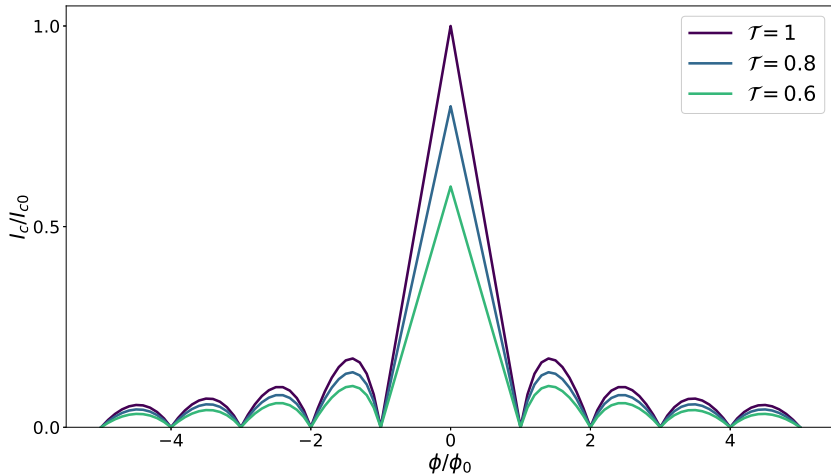


Figure 5.3: The normed critical current I_c/I_0 versus ϕ/ϕ_0 for different transmissions coefficients \mathcal{T} . For $\mathcal{T} > 1$, the barrier becomes reflective and the overall current density is low. The sharp peak at ϕ/ϕ_0 arises from the

where $\sin \tilde{\chi}$ has been rearranged in term of trigonometric functions. Since the integration is symmetric in the limits, only the term with $\cos\left(\frac{\pi\phi}{W}(y_1 + y_2)\right)$ is being kept in the expression for the current. Maximizing the Josephson current with respect to χ gives $\sin \chi \rightarrow 1$.

The result for the critical current at zero temperature for the limits of a wide and narrow junction has been done in [11] and is found

$$I_c(\nu) = \frac{2ev_F}{\lambda_F L^2} \frac{(1 - \{\nu\})\{\nu\}}{|\nu|}, \quad W/L \gg 1 \quad (5.23)$$

$$I_c(\nu) = \frac{ev_F}{\lambda_F L^2} \frac{(1 - \{\nu/2\})^2 \{\nu/2\}^2}{|\nu/2|^2}, \quad W/L \ll 1 \quad (5.24)$$

where $\nu = \phi/\phi_0$ and $\mathcal{T} \approx 1$. The fractional part of ν is denoted with $\{\nu\}$. Depending on the geometry of the sample, in particular depending on the ratio W/L , the periodicity of the Fraunhofer pattern changes. For a wide junction ($W/L \gg 1$), the critical curve is periodic in ϕ/ϕ_0 . With a changing ratio, the periodicity changes. In the other limit of a narrow junction with $W/L \ll 1$, the Fraunhofer pattern has a $2\phi_0$ periodicity.

Including Scattering At The Boundaries

So far, straight trajectories connecting the two superconducting interfaces have been considered. A process that is possible in principle, is a trajectory of an electron that is scattered at a side boundary (at $y = \pm W/2$, see figure 5.1). It is clear that, especially in the case of a short and wide junction with $W \gg L$, these trajectories do not contribute as much as the straight trajectories. When a trajectory is scattered at, say, a point at the upper edge $(x, y) = (x_s, +W/2)$, the parametrisation for the angle describing the trajectory is

$$\tan \theta = \frac{\bar{y}_2 - y_1}{L} = \frac{W - y_2 - y_1}{L}. \quad (5.25)$$

In this parametrisation, the coordinate \bar{y}_2 is the mirror image of y_2 . For straight trajectories the vector potential \mathbf{A} does not give an additional contribution, which can be seen in eq. (5.20). The

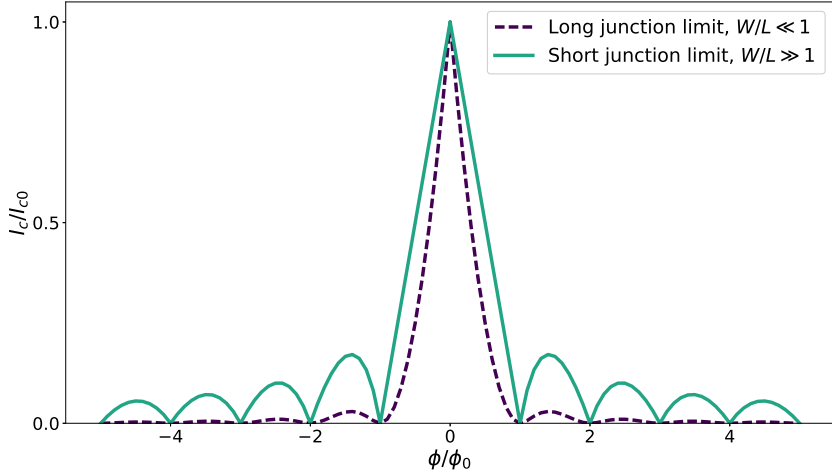


Figure 5.4: Normed critical current calculated from eqs. (5.24) and (5.23) for the long and short junction limit, respectively.

effective phase is in this case determined by eq. (5.15). When considering the scattering at side boundaries with the parametrization from eq. (5.25), the contribution from the magnetic phase is no longer zero,

$$\delta\chi = \frac{2\pi}{\Phi_0} \int_{-L/2}^{x_s} dx A_y(x) \tan \theta - \frac{2\pi}{\Phi_0} \int_{x_s}^{+L/2} dx A_y(x) \tan \theta \quad (5.26)$$

$$= -\frac{2\pi B}{\Phi_0} \tan \theta \left(\int_{-L/2}^{x_s} x dx - \int_{x_s}^{+L/2} dx \right) \quad (5.27)$$

$$= -\frac{2\pi B}{\Phi_0} \tan \theta \left(x_s^2 - (L/2)^2 \right) \quad (5.28)$$

$$= \frac{\pi\phi}{2W} \frac{(W-2y_1)(W-2y_2)}{W-y_1-y_2}, \quad (5.29)$$

since the trajectory changes the direction and therefore $d\mathbf{l} \cdot \mathbf{A}$ changes sign. The total effective phase difference is then, using eq. (5.15)

$$\tilde{\chi}(y_1, y_2) = \chi - \frac{\pi\phi}{2W} \left(2(y_1 + y_2) - \frac{(W-2y_1)(W-2y_2)}{W-y_1-y_2} \right) \quad (5.30)$$

With the contribution from side boundary scattering, the total Josephson current is

$$J(\chi, \phi) = J^{(0)}(\chi, \phi) + 2J^{(1)}(\chi, \phi). \quad (5.31)$$

$J^{(0)}$ denotes the part coming from straight trajectories. Since there are two side boundaries, the part describing the scattering, $J^{(1)}$, has an additional factor 2 and reads

$$J^{(1)} = \frac{2ev_F}{\pi\lambda_F L^2} \int \int_{-W/2}^{W/2} \frac{dy_1 dy_2}{\left[1 + \left(\frac{y_1-y_2}{L} \right)^2 \right]^2} \mathcal{J} \left(\chi - \frac{\pi\phi}{2W} \left(2(y_1 + y_2) - \frac{(W-2y_1)(W-2y_2)}{W-y_1-y_2} \right) \right) \quad (5.32)$$

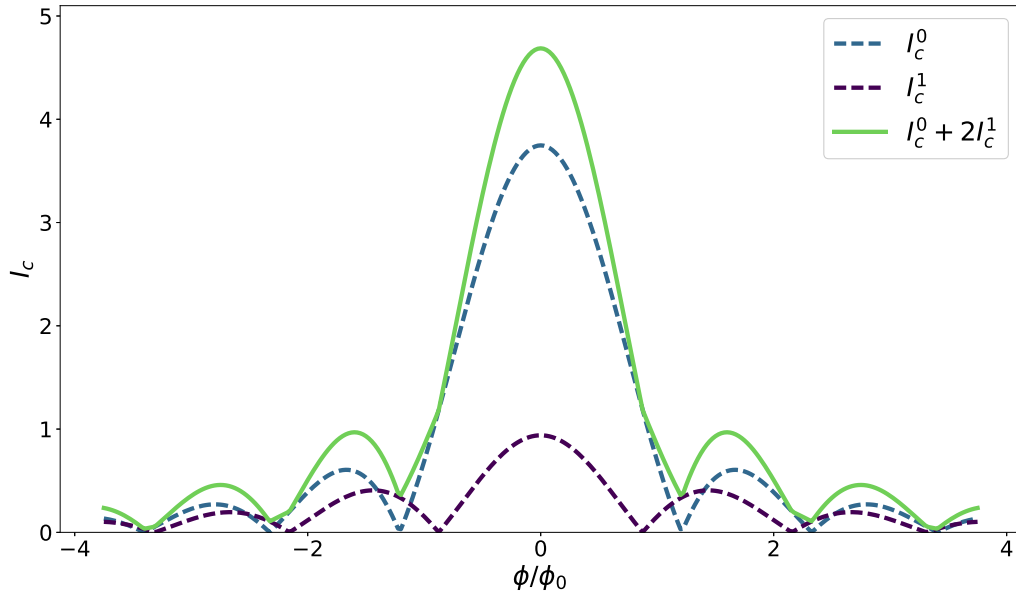


Figure 5.5: Comparison of contribution to current with and without boundary scattering at $T = 1$. The total current is a sum of the contribution without boundary scattering, $I_c^{(0)}$, and two times the current from the boundaries, $I_c^{(1)}$. The boundary scattering can be seen in the Fraunhofer pattern of the total current in the lifting of the lobes

This contribution has not been noted in [36]. In the case of short and wide junctions, it is sufficient to consider only $J^{(0)}$. For the cases, when $W/L \simeq 1$, it is necessary to sum over all possible edge channels. Figure 5.5 shows the result of equations (5.32) and (7.2). The overall contribution from the side scattering is lower than the contribution of only straight trajectories. In the total current, eq. (5.31), the edge scattering manifests by lifting the minimas from zero (see green curve in figure 5.5). This is in agreement with the results from [36]

5.3 Calculation Of The QPC Critical Current

The quasi classical formalism can even be employed to modified SNS junctions. One can build gates on top of the normal region of the junction in a way that the current cannot pass through the gated regions (see chapter 4). In the quasi classical picture, this means that the possibilities for trajectories connecting two points at the superconducting interfaces are limited through the geometry of the constriction.

Figure 5.6 shows a sketch of the quantum point contact set-up which will be analysed with the quasi classical formalism. The normal region of the SNS junction is covered by a gate with a small split in the middle. The split is located at $(x, y) = (0, 0)$ so that the sample is symmetric around the origin. The width of the split is in the order of λ_F and can thereby be viewed as an isotropic scattering point with transmission coefficient \mathcal{T}_0 . Trajectories connecting the two superconducting interfaces have to pass through the QPC. For simplicity, the geometrical width of the barrier is neglected, only straight trajectories are considered, and scattering at side edges is neglected. This modified set-up leads to a different parametrization of the trajectories and therefore to a different magnetic phase than in eq. (5.15).

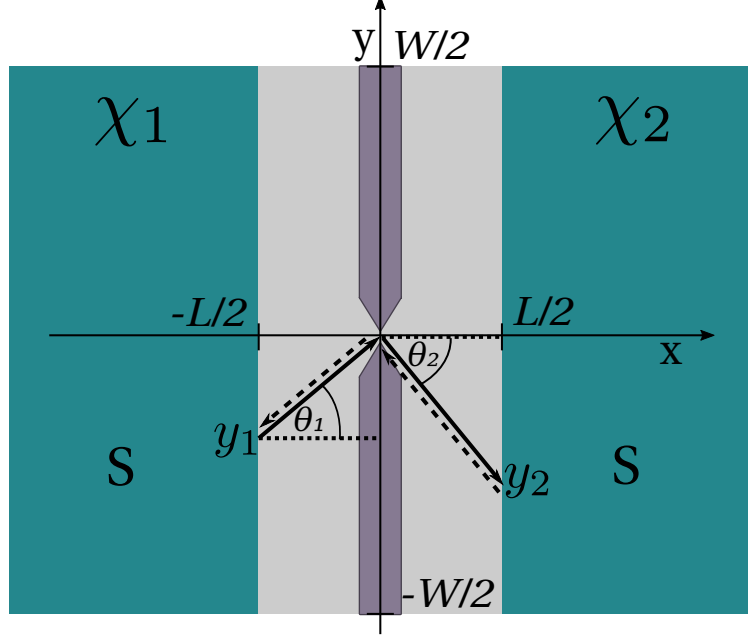


Figure 5.6: *SNS junction with a QPC gate on top. The split is located at $(x, y) = (0, 0)$, and the width of the barrier is assumed to be negligible. Each contributing trajectory has to pass through the origin. The angles θ_1 and θ_2 parametrize this trajectory.*

With the QPC set-up, all possible trajectories are parametrized by two angles θ_1 and θ_2 . θ_1 describes the trajectory before passing through the QPC in the region $-L/2 < x < 0$, and θ_2 after passing through the QPC. The parametrization of the trajectories reads

$$\tan \theta_1 = -\frac{2y_1}{L}, \quad \tan \theta_2 = \frac{2y_2}{L} \quad (5.33)$$

With the gauge from eq. (5.16), the magnetic phase acquired within the sample reads

$$\frac{2\pi}{\Phi_0} \int d\mathbf{l} \cdot \mathbf{A} = -\frac{\pi B}{\Phi_0} \left(\frac{L}{2} \right)^2 (-\tan \theta_1 + \tan \theta_2) = -\frac{\pi \phi(y_1 + y_2)}{2W}. \quad (5.34)$$

The total phase difference is the difference of the contribution coming from the magnetic field, eq. (5.34) and the superconducting phase difference eq. (5.15). The effective phase for the QPC set-up is found to be

$$\tilde{\chi}(y_1, y_2) = \chi - \frac{\pi \phi}{2W}(y_1 + y_2). \quad (5.35)$$

One consequence of the additional gate on top of the normal region is the change in the effective phase, resulting in a modified current phase relation $\mathcal{J}(\tilde{\chi}(y_1, y_2))$. Another consequence is a modified expression for the critical current. In the set-up without gates, straight trajectories with a fixed angle θ were considered and summed up to a total contribution. The difference in the QPC set-up is the split in the gate, which is modelled as an isotropic scattering point. The trajectories being summed up in this set-up can be thought to consist of two parts. The first part connects y_1 with the split at $(x, y) = (0, 0)$ and is determined by the direction of the trajectory. This explains the Fermi velocity in this part(?). The second part of the current trajectory starts from the origin and connects it with a point at the right interface y_2 . Summing up, the critical current in the QPC set-up is

$$I_c^{\text{QPC}}(\phi) \propto \max_{\chi} \int d\theta_1 v_F \cos^2 \theta_1 \int d\theta_f \cos \theta_f \mathcal{J}(\tilde{\chi}(\theta_1, \theta_2)) \quad (5.36)$$

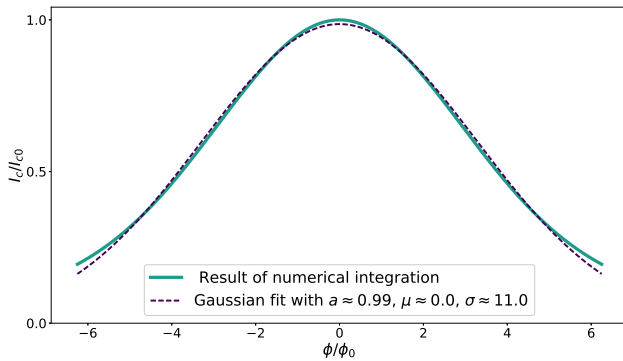


Figure 5.7: Plot of the numerical integration for the QPC current from eq. (5.37) and the result of the fitting to a Gaussian curve.

The QPC is modelled as an isotropic scatterer with transmission probability \mathcal{T} . If the transmission is small, $\mathcal{T} \ll 1$, eq. (5.12) can be used for \mathcal{J} . The angles $\theta_{1,2}$ can be rewritten in terms of $y_{1,2}$ by using the parametrization from eq. (5.33), allowing the normalized critical current to be expressed as

$$\frac{I_c(\phi)}{I_c(0)} = \frac{\mathcal{I}_2(\phi)\mathcal{I}_{3/2}(\phi)}{\mathcal{I}_2(0)\mathcal{I}_{3/2}(0)}, \quad (5.37)$$

where the integrals \mathcal{I} are defined as

$$\mathcal{I}_k(\phi) = \frac{2}{L} \int_{-W/2}^{+W/2} dy \frac{\cos\left(\frac{\pi\phi y}{2W}\right)}{\left[1 + \left(\frac{2y}{L}\right)^2\right]^k} \quad (5.38)$$

Evaluating the integral in eq. (5.37) numerically gives a bell-shaped form that is very well described with a Gaussian function $\exp(-a(x - \mu)^2/(2\sigma)^2)$. Figure 5.7 shows a plot of the resulting current from the integration as well as a plot of the fitted function.

Evaluation In Limits

The current can be evaluated in the limit of small flux $\phi \rightarrow 0$, and in limit of high fields $\phi \rightarrow \infty$. At $\phi = 0$ the cosine term becomes one leading to the simple expression

$$\mathcal{I}_2(0)\mathcal{I}_{3/2}(0) = \frac{2W^2 L}{(L^2 + W^2)^{3/2}} + \frac{2W}{\sqrt{L^2 + W^2}} \arctan \frac{W}{L} \quad (5.39)$$

$$\equiv \frac{2x^2}{(1+x^2)^{3/2}} + \frac{2x}{\sqrt{1+x^2}} \arctan x, \quad (5.40)$$

where $x \equiv W/L$. The parabolic asymptotics of the critical current at small ϕ is found by expanding the cosine factors in the numerator:

$$\frac{I_c(\phi)}{I_{c0}} \simeq 1 - \frac{\pi^2 \phi^2}{32} f_0(W/L) \quad (5.41)$$

$$f_0(x) = \frac{\sqrt{x^2 + 1} \log\left(\sqrt{x^2 + 1} + x\right)}{x^3} - \frac{2}{x(x + (x^2 + 1) \arctan x)} \quad (5.42)$$

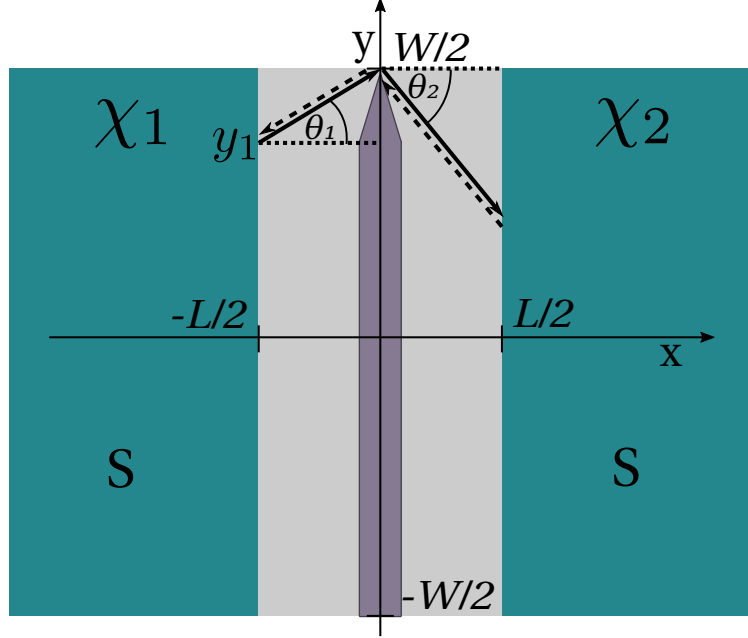


Figure 5.8: A SNS junction with split at upper edge, $(x, y) = (0, +W/2)$. Similar to the QPC set-up, this constriction is formed so that each trajectory has to pass through it in order to contribute to the current.

In the opposite limit of high fields, $\phi \rightarrow \infty$, the integration in eq. (5.38) is extended over y_1 and y_2 to $\pm\infty$ and obtain

$$\frac{I_c(\phi)}{I_{c0}} = \frac{\pi^{3/2}}{8x} \frac{(1+x^2)^{3/2}}{x + (1+x^2) \arctan x} \left(\frac{\pi\phi}{2x} \right)^{3/2} \exp \left(-\frac{\pi\phi}{2x} \right) \quad (5.43)$$

5.4 QPC Edge Current

The role of edge current is of importance when studying SNS junctions. As has been explained in chapter 4, when a large band gap is opened in BLG, an insulating state is expected, especially at very low temperatures. The non-occurrence of this insulating state has been attributed to the existence of edge currents in the sample. It makes sense to address the problem also for the QPC in within the quasi-classical framework. To this end, two scattering points at the edges $(x, y) = (0, \pm W/2)$ are introduced. These scattering points are modelled in the exact same way as the QPC (they are assumed to be isotropic scatterers) and only differ by means of transmission coefficient. The edge channel transmission coefficient is denoted with \mathcal{T}_e and the QPC transmission coefficient with \mathcal{T}_q .

The parametrization of an edge trajectory, illustrated in figure 5.8, reads

$$\tan \theta_1 = \frac{W - y_1}{L/2}, \quad \tan \theta_2 = -\frac{W - y_2}{L/2}. \quad (5.44)$$

Similar to the QPC contribution, the magnetic phase gain along the trajectory is calculated. For

the upper edge, the result is

$$\frac{2\pi}{\phi_0} \int d\mathbf{l} \cdot \mathbf{A} = \frac{2\pi}{\phi_0} \left(\int A_y(x) |d\mathbf{l}| |\mathbf{e}_y| \sin \theta_1 + \int A_y(x) |d\mathbf{l}| |\mathbf{e}_y| \sin \theta_2 \right) \quad (5.45)$$

$$= -\frac{2\pi B}{\phi_0} \left(\int_{-L/2}^0 x dx \tan \theta_1 + \int_0^{L/2} x dx \tan \theta_2 \right) \quad (5.46)$$

$$= -\frac{\pi B L}{\phi_0} \frac{1}{2} (-\tan \theta_1 + \tan \theta_2) \quad (5.47)$$

$$= -\frac{\pi B L}{\phi_0} \frac{1}{2} (-2W + (y_1 + y_2)) \quad (5.48)$$

$$= \pi \Phi - \frac{\pi \Phi}{2W} (y_1 + y_2), \quad (5.49)$$

where

$$\Phi = \frac{\phi}{\phi_0}, \quad \phi = BWL \quad (5.50)$$

has been used. Together with the contribution from the set-up without any constriction from eq. (5.15), the total phase for the edge transmission is added up to

$$\tilde{\chi}(y_1, y_2) = \chi - \frac{3\pi\Phi}{2\phi_0} (y_1 + y_2) + \pi\Phi. \quad (5.51)$$

This is the effective phase $\tilde{\chi}(y_1, y_2)$ for the upper edge leading to a critical current $I_c^{e,u}$. Analogously, the phase for the lower edge can be constructed with a simple sign change in the parametrization in eq. (5.44):

$$\tilde{\chi}(y_1, y_2) = \chi + \frac{3\pi\Phi}{2\phi_0} (y_1 + y_2) - \pi\Phi, \quad (5.52)$$

which is the effective phase for the lower edge current, $I_c^{e,l}$. The Josephson relation for the edge contribution has the modified phase from eq. (5.51). The result for the QPC in the limit in high fields, eq. (5.43), has a transmission coefficient $\mathcal{T} = 1$. For easier comparison with the edge channel contribution, this is rewritten into the following form

$$I_c^{\text{QPC}} = \mathcal{T}_q F(W/L), \quad (5.53)$$

where the function $F(W/L)$ represents the result from eq. (5.43). The integrals for the upper edge can be written in a similar way:

$$I_c^{e,u} = \mathcal{T}_e \max_{\chi} \left\{ \sin(\chi_0 - \pi\Phi) \int_0^\infty d\tilde{y}_1 \int_0^\infty d\tilde{y}_2 \frac{\cos\left(\frac{3\pi\Phi\tilde{y}_1}{2W}\right)}{\left(1 + \left(\frac{2\tilde{y}_1}{L}\right)^2\right)^2} \frac{\cos\left(\frac{3\pi\Phi\tilde{y}_2}{2W}\right)}{\left(1 + \left(\frac{2\tilde{y}_1}{L}\right)^2\right)^{3/2}} \right\} \quad (5.54)$$

$$= \mathcal{T}_e \max_{\chi} \left\{ \sin(\chi - \pi\Phi) \right\} \frac{F(W/L)}{4}, \quad (5.55)$$

where

$$\tilde{y}_{1/2} = W/2 - y_{1/2}. \quad (5.56)$$

The total critical though the junction is proportional to the sum of the individual contributions of the QPC, the upper edge, and the lower edge: $I_c^{\text{total}} = I_c^{\text{QPC}} + I_c^{e,u} + I_c^{e,l}$. The normalized total

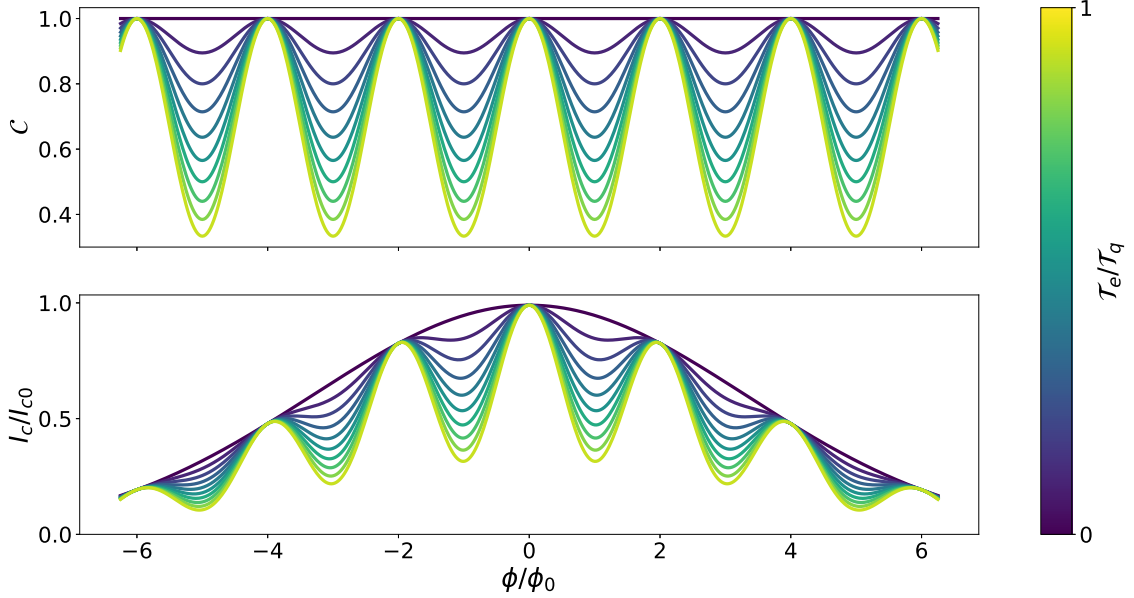


Figure 5.9: Upper plot: Correction factor C versus magnetic flux ϕ/ϕ_0 for different values of T_e/T_q . Lower plot: critical current for the QPC from eq. (5.37), modulated by C .

current then is

$$\frac{I_c^{\text{total}}(\phi)}{I_{c0}^{\text{total}}} = \max_{\chi} \left\{ \mathcal{T}_q \sin \chi + \frac{\mathcal{T}_e}{4} \sin (\chi - \pi\phi) + \frac{\mathcal{T}_e}{4} \sin (\chi + \pi\phi) \right\} / (\mathcal{T}_q + \mathcal{T}_e/2) \quad (5.57)$$

$$= \frac{|\mathcal{T}_q/\mathcal{T}_e + \cos(\pi\phi)/2|}{\mathcal{T}_q/\mathcal{T}_e + 1/2} \quad (5.58)$$

$$\equiv C \quad (5.59)$$

In figure 5.9 visualizes, how the total critical current is affected if edge channels are present. The color scale indicates the ratio of transmissions coefficients \mathcal{T}_e and \mathcal{T}_q . When $\mathcal{T}_e/\mathcal{T}_q \approx 1$, meaning the transmission of the edges is as strong as the transmission of the QPC, the current is strongly modulated and the bell-shaped pattern is destroyed. When the ratio is small, the Gaussian curve is not affected by the modulation. The data presented in chapter 4 in section 4.3 suggests that edge current do not have a major influence in this setup.

5.5 Barrier With Finite Split Width: Transition To The QPC Set-up

The QPC set-up and the SNS set-up without barriers can be linked conceptually by investigating an hourglass-shaped set-up. This set-up constricts the trajectories through a split with a finite width w_s as visualized in figure (5.10). When considering only straight trajectories, this split width models the transition to the QPC in the limit of $w_s \rightarrow 0$. The difference to the QPC is simply the parametrization of the angles: with a finite w_s , trajectories are parametrized by only one angle θ ,

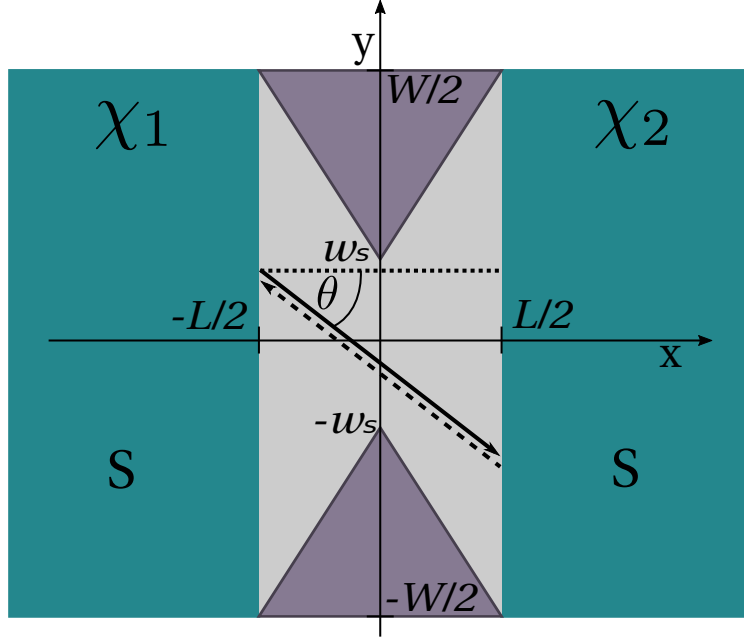


Figure 5.10: An SNS junction with hourglass-shaped constriction on top. The split is located at $(x, y) = (0, \pm w_s/2)$ and the trajectory is parametrized by the angle θ .

the direction does not change after passing the split:

$$J(\chi, \phi) = \frac{2ev_F}{\pi\lambda_F L^2} \int_{-W/2}^{W/2} dy_1 \int_{\theta_{\min}}^{\theta_{\max}} \frac{\mathcal{J}(\tilde{\chi}(y_1, y_2))}{\left(1 + \left(\frac{y_2 - y_1}{L}\right)^2\right)^2}, \quad (5.60)$$

where

$$\theta_{\min} = \arctan\left(-\frac{w_s + 2y_1}{L}\right), \quad (5.61)$$

$$\theta_{\max} = \arctan\left(\frac{w_s - 2y_1}{L}\right). \quad (5.62)$$

When w_s is small enough, like in the QPC case, two independent trajectories are considered with two parametrization angles θ_1 and θ_2 . This set-up is particularly interesting because the impact of asymmetry in the junction can be studied. When relocating the split by for example moving it along the x -axis, the possible trajectories are limited. As a consequence, the Fraunhofer pattern changes.

6 Numerical Results

6.1 QPC

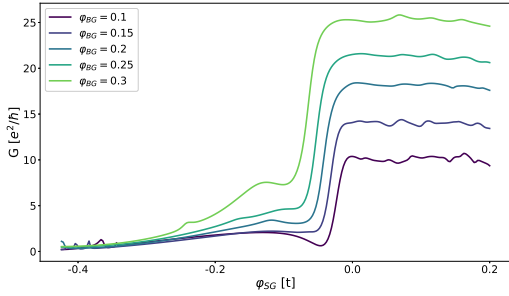


Figure 6.1: Conductance QPC

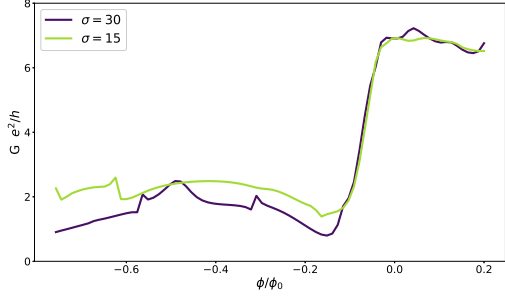


Figure 6.2: default

A fixed back-gate voltage leading to an n-doping of the scattering region is assumed, because the measurements of the experiment where conducted at fairly low charge carrier density. For increasingly negative values of the split-gate voltage, the region underneath the top gate becomes p-doped. The higher the split-gate voltage, the lower the transparency of the barrier becomes, and at a certain point, the current transport is confined to very few channels (see section 4.2). In figure 6.1, the conductance is plotted versus split-gate voltage. For increasingly negative values of the split-gate voltage, only few conducting channels remain. For the following calculations the back-gate voltage is chosen to be $\varphi_{BG} = 0.2$.

For increasingly positive back-gate voltage, the overall conductivity of the sample increases and the critical current cannot be confined.

The stray fields produced at the edges of the top-gate voltage are being considered as well since they are crucial for the conductive behaviour of the barrier. They are modelled as a gaussian filter applied to the vertical electric field lines:

$$g(x) = \frac{1}{\sqrt{2\pi}\sigma} e^{-\frac{x^2}{2\sigma^2}}. \quad (6.1)$$

Figure 6.2 shows two conductance lines for the same back-gate of $\varphi_{BG} = 0.2$, differing only in their σ values. For very high values of σ , the QPC stops to function as a confinement of the current, but becomes an entirely reflective barrier. For $\sigma = 30$, the conductance falls below the threshold of 1.

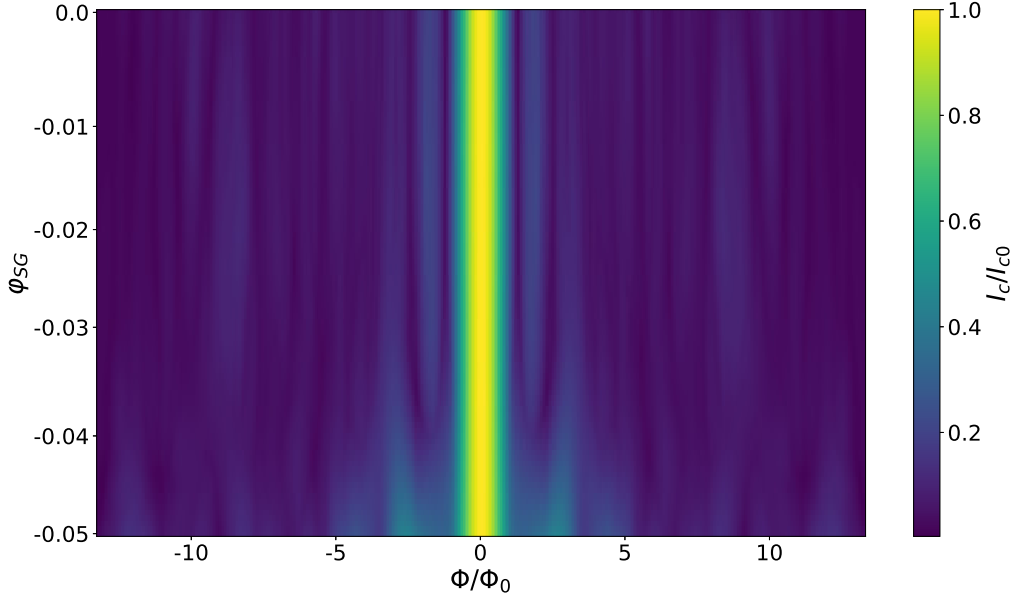


Figure 6.3: The normed critical current I_c^{norm} as a function of quantised flux and split-gate voltage φ_{SG} .

Figure 6.3 shows the supercurrent that has been simulated by the procedure presented in 3.2.2. The normed critical current is displayed as the heat color. It is plotted against the normed flux for different split-gate potentials. One can see clearly that for a split-gate potential of approximately 0 – a transmissive barrier – the critical current has the form of a Fraunhofer-like beating pattern. With increasing split-gate potential, the barrier becomes increasingly reflective, a constriction is formed, and the current is confined. A bell-shaped pattern is observed. This corresponds well to the findings presented in 4. It should be noted that the transition from beating pattern to bell-shaped pattern happens on a narrow range of the split-gate potential.

6.2 Half-Barrier

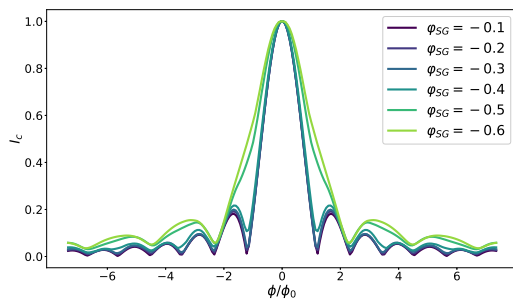


Figure 6.4: HB normalized current

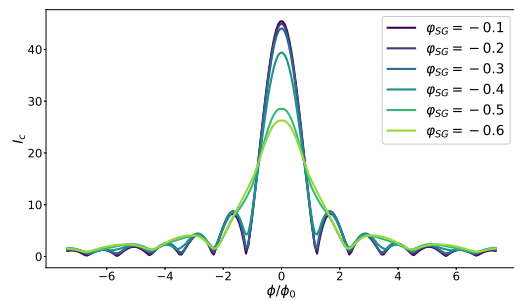


Figure 6.5: HB current

The two fingers of the QPC experiment can be tuned individually, so measurements of in-

dividually gated (half-barrier) set-ups were included in the experimental set-up. As of yet, no measurement data has been published, though.

The simulations have been carried out with a higher back-gate potential, which explains the higher values of the split-gate potential in the following plots. It is not important to have a low charge carrier density, because this set-up does not aim to confine the current. A back-gate potential of as high as $\varphi_{BG} = 0.8$ has been chosen.

The plot in figure 6.5 shows that when the barrier is fully formed, I_{c0} is halved compared to its value when there is no split-gate. Figure 6.4 illustrates that as the barrier forms, the periodicity of the pattern almost doubles. This behaviour is observed in the experiment as well.

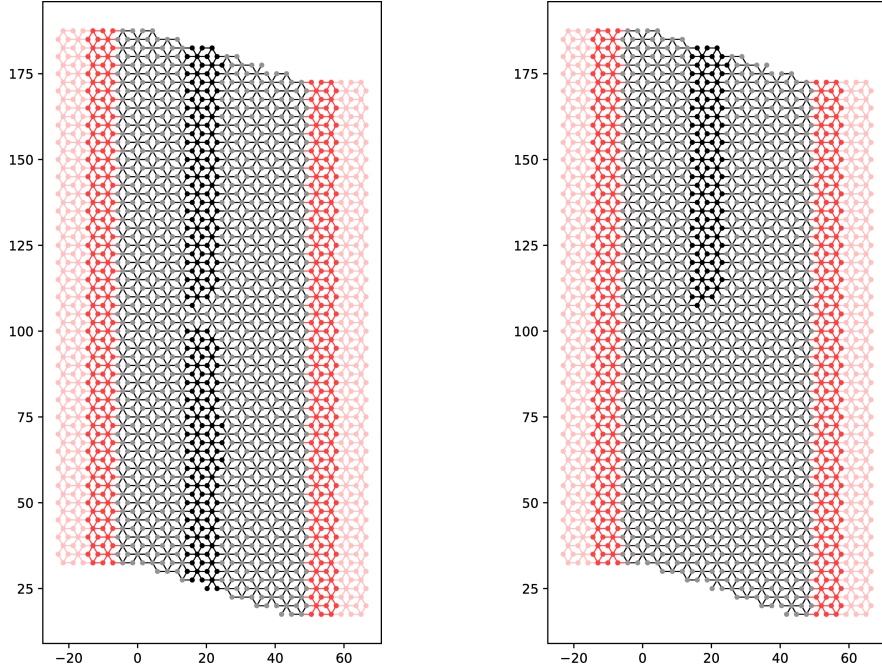


Figure 6.6: *Systems*

The halving of the critical current peak can be explained within the framework of the quasi-classical theory. When a barrier is fully present, only half of the trajectories connecting the superconducting leads can pass. Figure 6.6 pictures the implementation of the sample in `kwant`. The geometry of the asymmetric sample manifests in the Fraunhofer pattern. Because of the asymmetry, the upper finger allows for more trajectories than the lower finger. The maximum current therefore saturates at a higher threshold with the upper half-barrier.

Periodicity can be understood geometrically as well: About half of the area contributes to the magnetic phase. The phase changes accordingly, which leads to a doubling of the periodicity.

6.3 Wave-guide

The wave-guide set-up of figure 6.7 is, again, a short and wide junction with a narrow channel of $1 \mu m$. The current can be confined similarly to the QPC set-up. Because of the wide channel, the value for the high back-gate potential can be chosen to be relatively high. This is justifiable, since in comparison to the QPC set-up, the waveguide set-up is measured experimentally at higher charge carrier densities. The advantage of this set-up is the translation invariance in the x-direction because of its symmetry. This allows for fourier transformation of the current with the method of Dynes and Fulton [37].

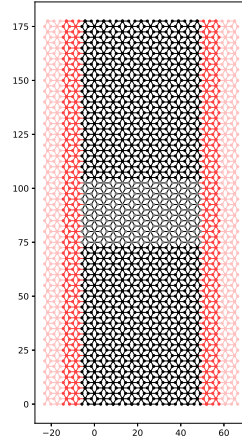


Figure 6.7: Waveguide system

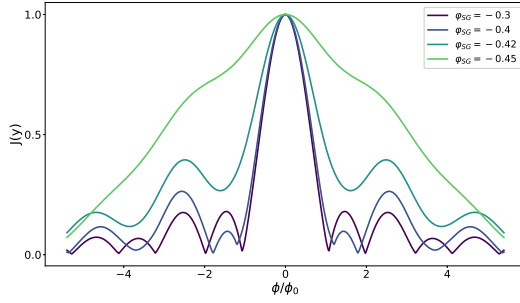


Figure 6.8: Conductance QPC

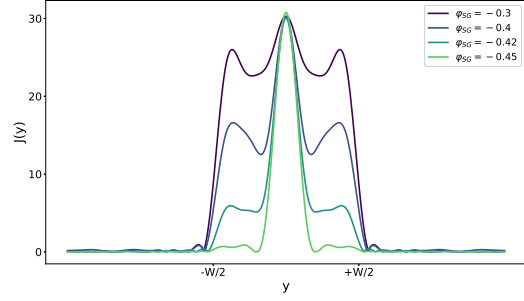


Figure 6.9: default

Figure 6.8 shows the normalized critical current. Similar to the results of the QPC simulation, a transition to a bell-shaped pattern can be observed. By fourier transforming the I_c -curves, the current density distribution along the width of the junction can be obtained. This current distribution is shown in figure 6.9. For low values of the split-gate potential, the current density distribution is approximately rectangular. This implies that there is current flow below the top-gates. When the values of the split-gate potential become increasingly negative, the current density distribution resembles a sharp peak. In this situation, the current transport is confined to the area not covered by the top-gate.

7

Conclusion And Outlook

Results

The central result of this work is that

$$J(\tilde{\chi}(y_1, y_2), \phi) \propto \int \int_{-W/2}^{W/2} dy_1 dy_2 \frac{\mathcal{J}(\tilde{\chi}(y_1, y_2))}{\left(1 - \left(\frac{y_1 - y_2}{L}\right)^2\right)^2} \quad (7.1)$$

The denominator for a current through SNS junction goes with a power of 2. This contradicts the result of [11]. The current density for the QPC has been established, it reads

$$J(\tilde{\chi}(y_1, y_2), \phi) \propto \int \int_{-W/2}^{W/2} dy_1 dy_2 \frac{\cos\left(\frac{\pi\phi}{W}(y_1 + y_2)\right)}{\left[1 + \left(\frac{y_1 - y_2}{L}\right)^2\right]^2}, \quad (7.2)$$

The critical current was evaluated for the $\phi \rightarrow 0$ boundary case where a parabolic function dependent on W/L was found for the QPC. In the other boundary case, $\phi \rightarrow \infty$, the exponential decline for large ϕ is correctly reproduced. The behaviour of the boundary currents was also investigated within the framework of the quasi-classical approximation. It is shown that for different coefficients of transmittance \mathcal{T}_e of the edge and \mathcal{T}_q of the QPC the critical current is modulated by a factor

$$\mathcal{C} = \frac{|\mathcal{T}_q/\mathcal{T}_e + \cos(\pi\phi)/2|}{\mathcal{T}_q/\mathcal{T}_e + 1/2}. \quad (7.3)$$

This modulation is already visible with values of around $\mathcal{T}_e/\mathcal{T}_q = 1/100$. This is a strong indication that there are no edge streams in the observed data.

Outlook

The transport theory presented in the scope of this thesis can be expanded in various aspects. It was demonstrated that this theory can model a *weak link* in the form of a QPC fairly well. It is therefore conceivable to model other, similar forms of weak links.

In this thesis, a short SNS-set-up was considered. As a consequence, certain approximations that simplify the calculations have been made. For the other boundary case of a long SNS junction, scattering at the edges is an important component for current transport and must therefore be taken into account. Secondly, higher-order terms must be considered when calculating the current density. Thus, the simplest form of the Josephson equation is no longer sufficient in this case.

7 Conclusion And Outlook

So far, only Andreev retro-reflexion has been considered, where the hole is reflected on approximately the same trajectory as the electron, only with inverted impulse. In the case of graphene, however, the process is dominated by the specular Andreev reflection, in which the reflected hole does not return on the same trajectory. The quasi-classical theory can also be extended to this case and thus consider graphene-specific properties.

The numerical simulations with **kwant** can be extended. This thesis work implements the BLG system as a de facto two-dimensional system. However, realistic experimental set-ups are more complex: On the one hand, they are three-dimensional, and on the other hand, the assumptions of the spatial distribution of electrostatic fields so far are too simplistic. A combination of calculating these fields with numerical methods and simulations with **kwant** will allow for a more complete modelling of the experiments.

Bibliography

- [1] N. D. Mermin and H. Wagner. Absence of Ferromagnetism or Antiferromagnetism in One- or Two-Dimensional Isotropic Heisenberg Models. *Physical Review Letters*, 17(22):1133–1136, nov 1966.
- [2] K S Novoselov et al. Electric field effect in atomically thin carbon films. *Science (New York, N.Y.)*, 306(5696):666–9, oct 2004.
- [3] Yuanbo Zhang et al. Experimental observation of the quantum Hall effect and Berry’s phase in graphene. *Nature*, 438(7065):201–204, nov 2005.
- [4] K. S. Novoselov et al. Two-dimensional gas of massless Dirac fermions in graphene. *Nature*, 438(7065):197–200, nov 2005.
- [5] Gordon W. Semenoff. Condensed-Matter Simulation of a Three-Dimensional Anomaly. *Physical Review Letters*, 53(26):2449–2452, dec 1984.
- [6] Izabela Jurewicz et al. Insulator-Conductor Type Transitions in Graphene-Modified Silver Nanowire Networks: A Route to Inexpensive Transparent Conductors. *Advanced Functional Materials*, 24(48):7580–7587, dec 2014.
- [7] In Hyuk Son et al. Graphene balls for lithium rechargeable batteries with fast charging and high volumetric energy densities. *Nature Communications*, 8(1):1561, dec 2017.
- [8] M. I. Katsnelson, K. S. Novoselov and A. K. Geim. Chiral tunnelling and the Klein paradox in Å graphene. *Nature Physics*, 2(9):620–625, sep 2006.
- [9] M. J. Zhu et al. Edge currents shunt the insulating bulk in gapped graphene. *Nature Communications*, 8:14552, feb 2017.
- [10] Rainer Kraft et al. Tailoring supercurrent confinement in graphene bilayer weak links. feb 2017.
- [11] Victor Barzykin and Alexandre M. Zagoskin. Coherent transport and nonlocality in mesoscopic SNS junctions: Anomalous magnetic interference patterns. *Superlattices and Microstructures*, 25(5):797–807, 1999.
- [12] P. R. Wallace. The Band Theory of Graphite. *Physical Review*, 71(9):622–634, may 1947.
- [13] J. Bardeen, L. N. Cooper and J. R. Schrieffer. Theory of Superconductivity. *Physical Review*, 108(5):1175–1204, dec 1957.
- [14] B.D. Josephson. Possible new effects in superconductive tunnelling. *Physics Letters*, 1(7): 251–253, jul 1962.
- [15] Akira Furusaki. Josephson current carried by Andreev levels in superconducting quantum point contacts. *Superlattices and Microstructures*, 25(5-6):809–818, may 1999.
- [16] C. W. J. Beenakker. Specular Andreev reflection in graphene. apr 2006.

Bibliography

- [17] Dmitri K. Efetov and Konstantin B. Efetov. Crossover from retro to specular Andreev reflections in bilayer graphene. *Physical Review B*, 94(7), 2016.
- [18] Edward McCann and Mikito Koshino. The electronic properties of bilayer graphene. may 2012.
- [19] A. H. Castro Neto et al. The electronic properties of graphene. *Reviews of Modern Physics*, 81(1):109–162, jan 2009.
- [20] M.S. Dresselhaus, G. Dresselhaus and R. Saito. Physics of carbon nanotubes. *Carbon*, 33(7):883–891, jan 1995.
- [21] J. W. McClure. Band Structure of Graphite and de Haas-van Alphen Effect. *Physical Review*, 108(3):612–618, nov 1957.
- [22] J. W. McClure. Theory of Diamagnetism of Graphite. *Physical Review*, 119(2):606–613, jul 1960.
- [23] M Mucha-Kruczynski, E McCann and Vladimir I Fal’ko. Electron hole asymmetry and energy gaps in bilayer graphene. *Semiconductor Science and Technology*, 25(3):033001, mar 2010.
- [24] L. M. Malard et al. Probing the Electronic Structure of Bilayer Graphene by Raman Scattering. aug 2007.
- [25] A. B. Kuzmenko et al. Determination of the gate-tunable band gap and tight-binding parameters in bilayer graphene using infrared spectroscopy. *Physical Review B*, 80(16):165406, oct 2009.
- [26] Christoph W Groth et al. Kwant: a software package for quantum transport. *New Journal of Physics*, 16(6):063065, jun 2014.
- [27] Pier A. Mello, Pedro Pereyra and Narendra Kumar. A soluble random-matrix model for relaxation in quantum systems. *Journal of Statistical Physics*, 51(1-2):77–94, apr 1988.
- [28] C. W. J. Beenakker. Three Universal Mesoscopic Josephson Effects. 1992.
- [29] C. W J Beenakker and H. Van Houten. Josephson current through a superconducting quantum point contact shorter than the coherence length. *Physical Review Letters*, 66(23):3056–3059, 1991.
- [30] K. K. Likharev. Superconducting weak links. *Reviews of Modern Physics*, 51(1):101–159, jan 1979.
- [31] Edward McCann. Asymmetry gap in the electronic band structure of bilayer graphene. *Physical Review B*, 74(16):161403, oct 2006.
- [32] Jeroen B. Oostinga et al. Gate-induced insulating state in bilayer graphene devices. *Nature Materials*, 7(2):151–157, feb 2008.
- [33] Thiti Taychatanapat and Pablo Jarillo-Herrero. Electronic Transport in Dual-gated Bilayer Graphene at Large Displacement Fields. sep 2010.
- [34] F. Chiodi et al. Geometry-related magnetic interference patterns in long SNS Josephson junctions. jan 2012.

Bibliography

- [35] Alexandre M. Zagorskin. The half-periodic Josephson effect in an s-wave superconductor-normal-metal-d-wave superconductor junction. *Journal of Physics Condensed Matter*, 9(31), 1997.
- [36] Hendrik Meier, Vladimir I. Fal'Ko and Leonid I. Glazman. Edge effects in the magnetic interference pattern of a ballistic SNS junction. *Physical Review B*, 93(18):1–13, 2016.
- [37] R. C. Dynes and T. A. Fulton. Supercurrent Density Distribution in Josephson Junctions. *Physical Review B*, 3(9):3015–3023, may 1971.